Mitigating readout errors in superconducting qubit devices

Zur Erlangung des akademischen Grades eines

Doktors der Naturwissenschaften (Dr. rer. nat.)

von der KIT-Fakultät für Physik des

Karlsruher Instituts für Technologie (KIT)

genehmigte

Dissertation

von

M.Sc. Andras Di Giovanni

Tag der mündlichen Prüfung:	09.05.2025
Referent:	Prof. Dr. Alexey V. Ustinov
Korreferent:	Prof. Dr. Martin Gärttner

Contents

1 Introduction

Quantum machines have started to change our world. Atomic force microscopes can probe cell membranes and find defects on surfaces with unforeseen precision [1]. Magnetic resonance imaging identifies early cancer every day in a non-invasive way [2]. Josephson parametric amplifiers can increase electromagnetic signals by multiple orders of magnitude, while barely adding more noise than the quantum limit [3]. Superconducting quantum interference devices (SQUIDs) can sense minuscule changes in magnetic field, enabling spatial imaging of brain activity in the human brain [4]. However, the laws of quantum mechanics allow for the construction of a quantum machine that can change our world as we know it in ways that we do not currently comprehend. Richard Feynman, an American drummer, prankster and lock-picker [1] who first expressed the possibility and need for such a machine called it a quantum computer: “Nature isn’t classical, dammit, and if you want to make a simulation of nature, you’d better make it quantum mechanical, and by golly it’s a wonderful problem, because it doesn’t look so easy.” [5]. Since then, much progress has been made [6, 7], but a generally useful machine is still likely decades away.

In this thesis, I present methods, experiments, results and discussions on one of the key challenges that are part of the "how do we build it?" question. A second, equally important question is what to do with a general fault-tolerant quantum computer once built. This question, however, will not be investigated here.

The practical realization of quantum computing hardware has rapidly evolved over the past two decades, with superconducting qubits emerging as one of the most promising platforms due to their scalability, controllability, and compatibility with existing microfabrication technologies [6]. A further advantage is their fast gate and readout operations [8, 9]. Superconducting qubits operate based on Josephson junction circuits cooled to cryogenic temperatures, allowing coherent manipulation and entanglement through microwave and magnetic flux pulses [6, 7]. The indirect measurement approach commonly used in superconducting qubits

[1] He was also a Nobel prize-winning theoretical physicist at Caltech

involves coupling each qubit dispersively to a resonator whose frequency shift encodes the qubit's state [10].

Despite these advantages, superconducting qubit systems face significant challenges even before scaling beyond noisy intermediate-scale quantum (NISQ) processors [7]. One bottleneck arises from qubit readout, traditionally implemented by coupling each resonator-qubit pair individually to dedicated microwave transmission lines. While straightforward, this approach becomes impractical at scale due to space constraints within cryogenic environments and the complexity of managing numerous microwave cables and amplifier chains. To address this issue, multiplexed readout schemes have been developed, allowing multiple resonators to share a single transmission line [11]. Multiplexing significantly reduces hardware complexity; however, it introduces new challenges such as readout crosstalk between resonators and reduced single-shot assignment fidelity due to amplifier saturation effects.

Readout errors manifest as discrepancies between the true quantum state of a system and its measured outcome distribution. They can be characterized through a confusion matrix — a probability matrix describing measurement outcomes given true states — which can be inverted or otherwise processed to mitigate errors in measured results [12]. Classical post-processing techniques based on detector tomography have been extensively explored in recent years for mitigating readout errors [13–15]. Detector tomography experimentally reconstructs the positive operator-valued measure (POVM) associated with the measurement process itself, providing detailed insights into measurement imperfections and enabling more accurate mitigation strategies [14].

Early demonstrations of detector tomography highlighted its potential for accurately characterizing measurement devices in optical systems [16]. Subsequent studies extended these methods to superconducting qubits [14].

Beyond classical post-processing methods, active error mitigation approaches have also been developed. These include techniques such as bit-flip averaging methods that systematically average out biases caused by asymmetric bit-flip errors during measurement [12]. Furthermore, machine learning-based approaches have received attention for their ability to adaptively mitigate readout errors; in Ref. [17], for example, deep neural networks were used to improve the discrimination of qubit states.

This thesis builds upon these foundational works and explores some novel research directions building especially on detector tomography. In particular, three main studies were conducted.

First, we study the resilience of readout error mitigation in the context of quantum state tomography on different readout noise sources and show significant improvements — up to 30x — in quantum infidelity.

Second, we construct a novel quality metric for multiplexed readout that goes beyond assignment fidelity in the sense that it is not limited to computational basis states and directly characterizes the speed at which quantum information is converted to classical information.

Third, we study a strongly readout-correlated system of two qubits and probe its dependence on the individual readout amplitudes. By constructing a correlation-conscious readout quality metric, we show that readout correlations can be efficiently suppressed without significantly affecting assignment fidelity in this system.

Ultimately, realizing practical large-scale quantum computers needs addressing both readout errors at the single-shot level and mitigating correlated noise effects arising from multiplexed readout. This thesis contributes toward the second goal by studying correlated errors within multiplexed readout schemes and introducing first optimization methods aimed at suppressing them.

The structure of the monograph is as follows: Chapter 2 provides the quantum information background necessary to understand the subsequent experiments and data analysis. Chapter 3 contains the description of the experimental setup used to control and read out the qubits as well as the description of how experiments are executed. Chapter 4 details the results of the first important experiment: the noise resilience benchmarking of the applied readout error mitigation protocol on a single qubit. Chapter 5 generalizes the concepts developed in Chapter 4 to a four-qubit system, introducing a novel readout metric beyond assignment fidelity. Chapter 6 applies the research from Chapters 4 and 5 to construct a readout metric which optimizes both assignment fidelity and readout correlations simultaneously. Finally, concluding remarks as well some ideas for further research building on this thesis are given in Chapter 7.

I wish the highly esteemed reader a positive experience. Be open but be critical, and don't hesitate to get in touch if any errors or mistakes are discovered - when you read (out) this thesis. I will gladly mitigate.

2 Theoretical background

This chapter provides the necessary quantum information background to understand the experiments and results in the subsequent sections. We first give a brief introduction into the vector formalism of quantum mechanics, particularly in the context of qubit theory, then discuss sources of errors in quantum computing and strategies to correct them. We then focus on more specialized theory frameworks relating to readout error mitigation, such as positive operator-valued measure formalism, quantum state tomography, quantum detector tomography and infidelity. These sections follow closely the theoretical sections in Ref. [18] and Ref. [19]. Finally, we turn to readout errors, including the concept of correlated readout errors and explain some of the basic readout quality metrics widely used in the superconducting qubit community.

2.1 Brief overview of quantum mechanics

Quantum mechanics provides a mathematical framework to describe the behavior of physical systems at the quantum scale. Central to this framework are the concepts of state vectors, Hilbert spaces, and density matrices, which together allow for the representation and analysis of quantum states. This section follows closely the more in-depth discussion of Ref. [20].

2.1.1 State Vectors

A state vector is a mathematical object that represents the state of a quantum system. It is denoted as

$$|\psi\rangle$$

and resides in a complex vector space. The state vector contains all the information about the system and allows us to compute probabilities of measurement outcomes and predict how the system evolves.

For a quantum system, the state vector is typically expressed as a linear combination of basis states:

$$|\psi\rangle = \sum_i c_i |i\rangle,$$

where $|i\rangle$ are orthonormal basis vectors, and c_i are complex coefficients known as probability amplitudes. The normalization condition

$$\sum_i |c_i|^2 = 1$$

ensures that the total probability of all possible outcomes of a measurement is equal to 1.

State vectors are used to describe pure states, which represent maximum knowledge about a quantum system at a specific point in time. They form the foundation for understanding quantum superposition, interference, and other phenomena.

2.1.2 Hilbert Space

The Hilbert space is the mathematical structure in which quantum states (state vectors) reside. It is a complete complex vector space equipped with an inner product that defines notions such as length and angle between vectors. The inner product between two vectors $|\psi\rangle$ and $|\phi\rangle$ is denoted by $\langle\psi|\phi\rangle$, and it provides information about their overlap or similarity. Any Hilbert space has an orthonormal basis $\{|i\rangle\}$ such that any state vector can be expressed as a linear combination of these basis states. The evolution of quantum systems is described by unitary operators on this space, governed by the time-dependent Schrödinger equation:

$$\mathrm{i}\hbar \frac{d}{dt} |\Psi(t)\rangle = \hat{H} |\Psi(t)\rangle \tag{2.1}$$

2.1.3 Density Matrices

While state vectors describe pure states, many quantum systems require a more general representation known as density matrices. A density matrix ρ encodes both pure states and mixed states (statistical mixtures of different quantum states). For a pure state $|\psi\rangle$, the density matrix is given by:

$$\rho = |\psi\rangle\langle\psi|.$$

For mixed states, which arise when there is uncertainty or statistical mixing in the system's preparation, the density matrix takes the form:

$$\rho = \sum_i p_i |\psi_i\rangle\langle\psi_i|,$$

where p_i are probabilities associated with each pure state $|\psi_i\rangle$ in the ensemble. The density matrix satisfies two key properties:

1. Hermiticity: $\rho = \rho^\dagger$
2. Trace Condition: $\mathrm{Tr}(\rho) = 1$.
3. Positive semi-definitiveness: the eigenvalues of ρ are non-negative

Density matrices are essential for describing open quantum systems interacting with their environment or systems where only partial information about the state is available.

Together, state vectors, Hilbert spaces, and density matrices provide a comprehensive mathematical framework for describing quantum systems. They allow us to model both isolated systems (pure states) and systems subject to noise or uncertainty (mixed states), forming the foundation for modern quantum mechanics.

2.2 Quantum bits

In classical computing, a bit represents the smallest unit of information. It can take the value of either 0 or 1. At any given time it is in exactly one of these classical states. In contrast, qubits (quantum bits) are objects that can hold information in the qubit Hilbert space spanned by its eigenstates. The vector-formulation of a single general qubit state $|\psi\rangle$ is:

$$|\psi\rangle = \alpha\,|0\rangle + \beta\,|1\rangle\,, \tag{2.2}$$

where:

- $|0\rangle$ and $|1\rangle$ are the two basis states
- $\alpha, \beta \in \mathbb{C}$ (i.e. they are both complex numbers),
- $|\alpha|^2 + |\beta|^2 = 1$ (normalization condition).

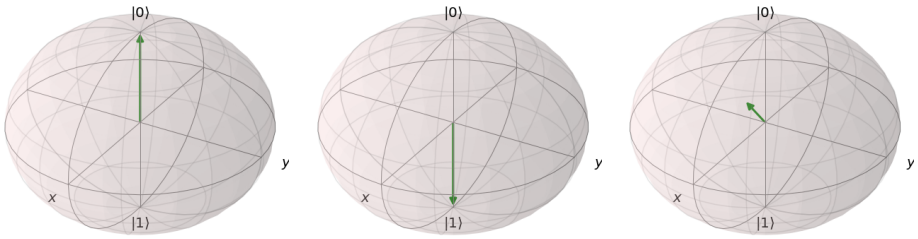

Figure 2.1: Bloch sphere representations of different single-qubit states Left: The ground state ($|0\rangle$ or spin state $|\uparrow\rangle$) of a qubit is represented by an arrow pointing to the north pole of a 2-sphere **Middle:** The excited state ($|1\rangle$ or spin state $|\downarrow\rangle$) is represented by an arrow pointing to the south pole **Right:** Qubits have the special property that the can take superposition states. These are states that are neither just $|0\rangle$, nor just $|1\rangle$, but an arbitrary complex combination, represented by an arrow pointing to any point on the surface of the Bloch sphere. Plotting done with QuTiP [23, 24].

In matrix form, $|\psi\rangle$ takes the form

$$|\psi\rangle = \begin{bmatrix} \alpha \\ \beta \end{bmatrix}.$$

For a single qubit with two eigenstates ($|0\rangle$ and $|1\rangle$ in the Z-basis), the Hilbert space is topologically equivalent to and thus often represented by a unit 2-sphere, where $|0\rangle$ is on the north pole, and $|1\rangle$ on the south pole. This sphere is called the Bloch sphere [21, 22]. In contrast to a classical bit, a qubit can take up quantum states that are anywhere on the Bloch sphere surface, which we represent by an arrow pointing from the centre of the sphere to a state on its surface. Three example quantum states (ground state, excited state and a superposition state) are shown in Fig. 2.1. Mixed states are located inside the Bloch sphere.

2.3 Dealing with errors in quantum computing

Quantum computing is prone to significant challenges due to errors arising from noise, decoherence, and imperfect operations [6, 25, 26]. Addressing these errors is crucial for advancing quantum technologies. This section discusses three key approaches: error correction, error mitigation, and readout error mitigation. The focus of the thesis is solely readout error mitigation, the other two techniques are very briefly introduced to give a broader picture of methods dealing with errors in quantum computers.

2.3.1 Error correction

Quantum error correction (QEC) [27–31] provides a robust framework for detecting and correcting errors by encoding logical qubits into multiple physical qubits. QEC actively protects quantum information against both bit-flip and phase-flip errors. Therefore, quantum error correction is currently seen as the method leading to fault-tolerance for future quantum computers.

Among QEC codes, the *surface code* stands out as one of the most promising due to its high fault-tolerance threshold and scalability. The surface code employs a 2D lattice of qubits arranged in a grid-like structure, with stabilizer measurements performed on neighboring qubits to detect and correct errors. Surface code based quantum error correction has been recently implemented in superconducting qubit devices [32–34].

The scalability of surface codes depends on achieving low physical error rates during gate operations and measurements. Advances in fabrication techniques and cryogenic systems have improved qubit coherence times and reduced gate errors, but further progress is needed to implement large-scale QEC systems. Efficient decoding algorithms are also critical for real-time error correction, as they must quickly identify and correct errors based on stabilizer measurement outcomes.

While surface codes impose significant hardware overhead, they represent a critical step toward fault-tolerant quantum computation. Once fully implemented, QEC is expected to enable reliable execution of complex algorithms on large-scale quantum processors.

2.3.2 Error mitigation

Error mitigation techniques aim to reduce the effects of noise in quantum computations without requiring additional qubits for encoding logical states. This is in contrast to error correction, which needs a physical qubit overhead and is thus more difficult to implement on near-term devices.

One widely used technique is *Pauli twirling* [35–38], which introduces controlled randomness into quantum operations. By applying random single-qubit Pauli gates before and after a noisy two-qubit operation, coherent errors are transformed into stochastic noise. This process simplifies the noise structure, making it easier to model and mitigate e.g. through post-processing. Pauli twirling is especially effective in reducing correlated errors that can otherwise propagate through a quantum circuit.

Another important approach is *zero-noise extrapolation* (ZNE) [39–44]. ZNE involves amplifying the noise in a controlled manner by scaling certain parameters of the quantum hardware, such as gate durations or control amplitudes. By measuring the outcome of the quantum computation at different noise levels and extrapolating the results back to the zero-noise limit, ZNE provides an effective way to estimate the expected outcome of a quantum computation if there had been no noise present in the system. While ZNE does not eliminate noise entirely, it significantly improves the accuracy of computations in noisy intermediate-scale quantum (NISQ) devices.

These error mitigation techniques are computationally efficient and do not require additional qubits, making them suitable for current-generation quantum processors.

2.3.3 Readout error mitigation

Readout errors occur during the measurement process when qubit states are incorrectly identified due to noise or imperfections in the measurement apparatus. These errors can significantly impact the accuracy of quantum experiments, particularly in tasks such as quantum state tomography.

Calibration-based techniques [14, 15, 18] are commonly used to mitigate readout errors. These methods involve characterizing the readout process by preparing known and easy-to-prepare input states and measuring their corresponding outputs. The resulting data is e.g. used to construct a confusion matrix that maps observed measurement frequencies to their true probabilities. By inverting this matrix during post-processing, measurement results can be mitigated against readout errors. One major assumption behind these methods is that quantum states can be prepared more precisely than they can be read out - an assumption that is valid for the vast majority of superconducting qubit processors. This makes calibration-based readout error mitigation methods particularly useful for this architecture.

The importance of readout error mitigation extends beyond NISQ devices; even in fault-tolerant systems, accurate measurements are essential for reliable operation.

2.4 Positive operator-valued measures (POVMs)

In the Copenhagen interpretation of quantum mechanics, the measurement of a system results in instantaneous wavefunction collapse. The superposition is lost, and the quantum state collapses into one of the eigenstates of the measurement

operator. Born's rule gives the expectation value of an operator O on the density matrix ρ of state:

$$\langle O \rangle = \mathrm{Tr}(\rho O) \tag{2.3}$$

An example of such an operator is the projective measurement of a qubit. The projection operator onto the ground state is $P_0 = |0\rangle \langle 0|$, the projection operator onto the excited state is $P_1 = |1\rangle \langle 1|$. The probability of collapsing onto each of the two basis states is therefore given by $p_i = \mathrm{Tr}(\rho P_i)$.

As the topic of the thesis is experimental readout error mitigation, we need a framework to describe imperfect measurements, which might not be fully projective. The framework of positive operator-valued measures (POVMs) describes generalized quantum measurements, such as the noisy readout of a superconducting qubit. A POVM is defined as a set of operators M_i, which are interpreted as yielding a probability distribution over measurement outcomes through their expectation values. The three defining properties of a POVM are as follows:

1. Hermiticity. M_i are Hermitian, guaranteeing real eigenvalues
2. Positivity. M_i are positive-definite. This is a weaker requirement than requiring all elements of the matrix to be positive, but implies positive expectation values.
3. Sum to identity. $\Sigma_i M_i = 1$, leading to the expectation values adding up to unity.

This framework allows one to assign a constituent operator M_i of the POVM to a single possible measurement of the experimental apparatus.

A notable example is the Pauli-6 POVM. Experimentally, this measurement is implemented by randomly selecting one of the x-, y-, or z-bases and performing a projective measurement in the chosen basis. The Pauli-6 POVM for a single qubit is defined by $\left\{ \frac{1}{3} |0_i\rangle \langle 0_i| , \frac{1}{3} |1_i\rangle \langle 1_i| \right\}$ where $\mathrm{i} \in \{\mathrm{x}, \mathrm{y}, \mathrm{z}\}$.

As an example, we given the two matrices (M_{z0} for outcome 0 and M_{z1} for outcome 1) constituting the ideal Z-readout projection operator for single qubit readout:

$$M_{z0} = \begin{bmatrix} 1+0i & 0+0i \\ 0+0i & 0+0i \end{bmatrix}, \quad M_{z1} = \begin{bmatrix} 0+0i & 0+0i \\ 0+0i & 1+0i \end{bmatrix}$$

The ideal two-qubit POVM matrices for XY-basis readout are:

$$M_{xy00} = \begin{bmatrix} 0.25+0i & 0-0.25i & 0.25+0i & 0-0.25i \\ 0+0.25i & 0.25+0i & 0+0.25i & 0.25+0i \\ 0.25+0i & 0-0.25i & 0.25+0i & 0-0.25i \\ 0+0.25i & 0.25+0i & 0+0.25i & 0.25+0i \end{bmatrix}$$

$$M_{xy01} = \begin{bmatrix} 0.25+0i & 0+0.25i & 0.25+0i & 0+0.25i \\ 0-0.25i & 0.25+0i & 0-0.25i & 0.25+0i \\ 0.25+0i & 0+0.25i & 0.25+0i & 0+0.25i \\ 0-0.25i & 0.25+0i & 0-0.25i & 0.25+0i \end{bmatrix}$$

$$M_{xy10} = \begin{bmatrix} 0.25+0i & 0-0.25i & -0.25+0i & 0+0.25i \\ 0+0.25i & 0.25+0i & 0-0.25i & -0.25+0i \\ -0.25+0i & 0+0.25i & 0.25+0i & 0-0.25i \\ 0-0.25i & -0.25+0i & 0+0.25i & 0.25+0i \end{bmatrix}$$

$$M_{xy11} = \begin{bmatrix} 0.25+0i & 0+0.25i & -0.25+0i & 0-0.25i \\ 0-0.25i & 0.25+0i & 0+0.25i & -0.25+0i \\ -0.25+0i & 0-0.25i & 0.25+0i & 0+0.25i \\ 0+0.25i & -0.25+0i & 0-0.25i & 0.25+0i \end{bmatrix}$$

Thus, a three-qubit POVM for a given readout basis (e.g. XXZ) would be a set of 8 complex matrices, where each of them has dimensions 8x8.

2.5 Quantum state tomography

As discussed above, the projective measurement of a quantum state destroys the possible superposition in that basis and thus most information in the quantum state is lost. To determine the full pre-measurement density matrix of the system, one needs to measure said state in multiple bases that span its Hilbert space. This requires the quantum state to be prepared multiple times.

The simplest approach to Quantum State Tomography (QST)[45] involves framing the problem as a linear inversion task, where the goal is to determine the density matrix from recorded measurement outcomes. However, linear inversion is often

criticized for producing unphysical estimates of quantum states [46]. Instead, estimators can be used, such as the Bayesian mean estimator (BME) [46, 47] or the maximum likelihood estimator (MLE) [48], both of which rely on the likelihood function [18]:

$$\mathcal{L}_M(\rho) \propto \prod_i \mathrm{Tr}(\rho M_i)^{n_i} = \left(\prod_i \mathrm{Tr}(\rho M_i)^{\hat{p}_i} \right)^N ,$$

where n_i is the number of times outcome i is observed, $\hat{p}_i = n_i/N$ is the outcome frequency, and M_i represents the POVM used in measurements. The likelihood function quantifies how likely the prepared state was ρ, given the observed outcomes. This way, as the likelihood function is only defined for physical states within the Hilbert space, physicality is explicitly guaranteed.

2.6 Quantum detector tomography

The experimental implementation of a positive operator-valued measure (POVM) is imperfect, therefore the assumption that one can perform a Z-basis projective readout is often not a suitable one. For an experimentalist[1], the problem statement that detector tomography aims to answer can be formulated as:

> *My measurement is not precise, because different noise sources bias it. Therefore, my measurement is not exactly what I would like it to be. But then, what is my measurement exactly?*

And the answer, given by the process of detector tomography becomes:

> *Prepare a set of quantum states very precisely, with errors much smaller than your readout imperfection. Now measure these states and see how the measured values are different from what you expected to measure on your near-perfect states. The offset you see is characteristic of your imperfect readout and can be used to find out exactly what your noisy readout process does.*

Now we turn to the rigorous definition of quantum detector tomography (QDT, [16]), i.e. the tomographic measurement of the quantum detector itself. This process directly reconstructs the POVM performed in the experiment based on observed

[1] The following explanation is intended to give an intuitive picture of detector tomography and is not mathematically rigorous.

results from a set of calibration states. Alternatively, QDT can be viewed as finding a map between the ideal and noisy POVMs,

$$\{M\} \to \{\tilde{M}\}.$$

This map can provide insights into noise parameters or the general behavior of the measurement device.

QDT begins by preparing a complete set of calibration states that span the entire quantum state space. Measurements are then repeatedly performed on these states. For instance, an (over)complete set of Pauli density operators,

$$\{|0_i\rangle \langle 0_i|, |1_i\rangle \langle 1_i|\}$$

with

$$i \in \{x, y, z\},$$

spans the space of single-qubit operators. Using the measurement outcomes, a linear system of equations can be constructed via Born's rule:

$$\frac{n_{is}}{N} = p_{is} = \mathrm{Tr}(\rho_s M_i), \tag{2.4}$$

where the subscript s indexes the set of calibration states, e.g.,

$$\{\rho_1 = |0_x\rangle\langle 0_x|, \rho_2 = |1_x\rangle\langle 1_x|, \dots\}.$$

Equation (2.4) imposes $I \times S$ constraints on the POVM elements $\{M_i\}$ to be reconstructed, where S is the number of unique calibration states and I is the number of POVM elements. Additionally, a normalization constraint applies to the effects:

$$\sum_i M_i = \mathbb{1}.$$

This formulation creates a statistical estimation problem similar to quantum state tomography. It can be solved using methods such as the maximum likelihood estimator outlined in Ref. [49], which ensures physically valid POVM reconstructions.

2.7 Infidelity between quantum states

To characterize the closeness of two quantum states, in particular two density matrices, we use the concept of quantum infidelity [20]. Thus, throughout the thesis, infidelity serves as an effective figure of merit for assessing the success of quantum state reconstruction. The goal is to minimize the infidelity, which is mathematically defined as:

$$I(\rho,\sigma) = 1 - F(\rho,\sigma) = 1 - \left[\mathrm{Tr}\left(\sqrt{\sqrt{\rho}\sigma\sqrt{\rho}}\right)\right]^2,$$

where $F(\rho,\sigma)$ represents the quantum fidelity. The square root of a density matrix, $\sqrt{\rho}$, is defined using its eigendecomposition:

$$\sqrt{\rho} = V\sqrt{D}V^{-1},$$

where

$$\sqrt{D} = \mathrm{diag}(\sqrt{\lambda_1}, \sqrt{\lambda_2}, \ldots, \sqrt{\lambda_n}),$$

with λ_i being the eigenvalues of ρ.

In this study, we focus exclusively on reconstructing pure target states (ρ), where the infidelity simplifies to:

$$I_{\mathrm{pure}}(\rho,\sigma) = 1 - \mathrm{Tr}(\rho\sigma).$$

2.8 Representation of readout errors

Errors that happen during or after a quantum computation that originate from inaccuracies or imperfections of the measurement process are called readout errors. A readout error can occur, for example, if the two computational basis states can not be perfectly distinguished from each other in an experiment. This could be caused e.g. by insufficient readout power or amplification [18]. This type of noise falls into the category of depolarizing noise, as it effectively shrinks the size of the Bloch sphere post-measurement, bringing the poles closer to each other. Another important type of readout error falls into the category of correlated readout errors. In practice, such errors can occur when multiplexed readout is performed and resonators are read out simultaneously with similar frequencies [50]. As a result, instead of performing the intended POVM $\{M_i\}$, the actual measurement

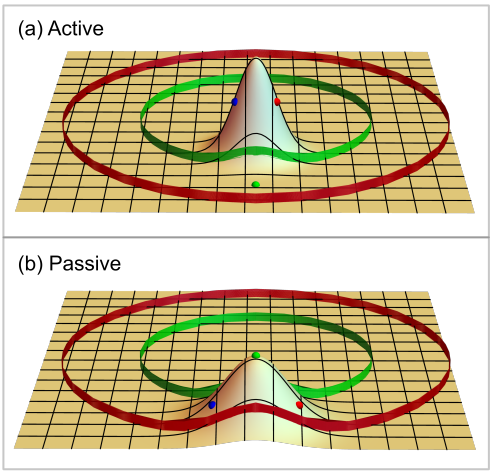

Figure 2.2: Active and passive noise pictures The likelihood function of a quantum state is plotted for a given step in quantum state reconstruction. For simplicity, only an intersection of the Bloch sphere with a horizontal plane is plotted (called a Bloch disk). The red ribbon represents the boundary of the Bloch disk, which is also the boundary of the Bloch sphere. This boundary shrinks when a depolarizing channel is applied (green ribbon). The true prepared state is marked in green. Due to depolarizing noise, its readout generates noisy data. The red and blue points represent two arbitrary states in their respective active and passive noise representations. **Top:** An unmitigated likelihood function in the active representation of noise. The reference states are very far away from the true state, reconstruction infidelity would be very low. **Bottom:** An error-mitigated likelihood function is presented in the passive representation of noise. The infidelity of reconstruction in this case would be very low. Image taken from Ref. [18].

corresponds to the erroneous POVM $\{\tilde{M}_i\}$. When measuring a quantum state ρ, the observed probability distribution follows Born's rule:

$$\tilde{p}_i = \mathrm{Tr}(\rho \tilde{M}_i),$$

which we refer to as the *passive* noise picture. Due to the cyclic property of the trace, the noise can be transferred to the quantum state instead, often called the *active* noise picture:

$$\tilde{p}_i = \mathrm{Tr}(\tilde{\rho} M_i),$$

where $\tilde{\rho}$ represents the ideal quantum state modified by a noise channel [20]. A visual representation of the two perspectives is shown in Fig. 2.2. Throughout the thesis, we will keep to the passive noise picture for the reason that by keeping the noise in the measurement operator, we can use detector tomography to estimate it.

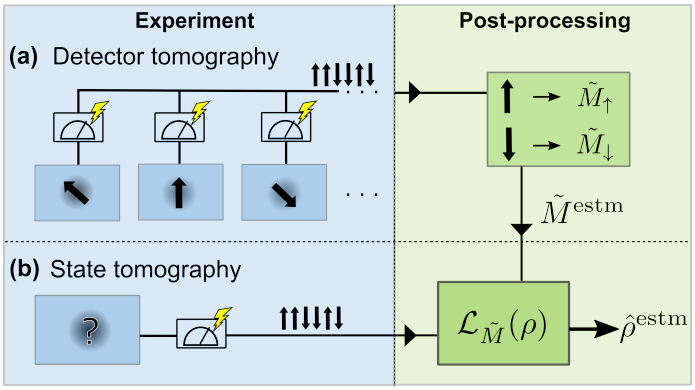

Figure 2.3: The readout error mitigation protocol used throughout this thesis. To reconstruct the readout error mitigated density matrix of a qubit, we first measure the action of a measurement applied to a set of well-known states. This allows one to estimate the effective POVM ($\tilde{M}^{estm}$) performed by the measurement device. This process is called detector tomography, or device tomography (DT), since it tomographically measures the action of the measurement process itself. Once $\tilde{M}^{\mathrm{estm}}$ is known, it can be applied in the quantum state tomography process to yield the readout error mitigated density matrix $\hat{\rho}^{\mathrm{estm}}$ [18].

2.9 Detector tomography based readout error mitigation

In this thesis we concern ourselves with readout error mitigation *in the context of quantum state tomography*. The protocol [18] applied and studied throughout this thesis is built up from two parts, see Fig. 2.3. First, quantum detector tomography is performed on the device, yielding estimates for the positive operator-valued measures effectively performed during readout. In the second step, a readout error-conscious state estimator is constructed which takes in measurement data in different bases. The estimator takes into account the fact that the measurements performed are imperfect, and uses the noisy, real measurement operators. This approach enables the reconstruction of the readout error mitigated density matrix of the prepared state. Using a Bayesian mean estimator enables one to extract infidelities on a shot-by-shot basis, which may be plotted in so-called infidelity curves. Some examples of infidelity curves for three different depolarizing noise strengths can be seen in Fig. 2.4. Examples of depolarizing noise investigated in this thesis are insufficient readout signal amplification and suboptimal resonator drive power.

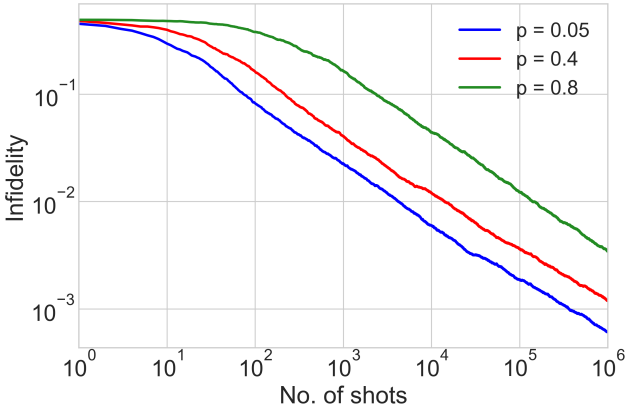

Figure 2.4: Infidelity convergence for readout error mitigated quantum state tomography in the presence of depolarizing noise Three different depolarizing strength values are plotted in different colours. The stronger the depolarizing noise, the less the computational basis state distinguishability of the readout, which leads to less information content in a single shot. This leads to slower convergence rates. Note that the plot is logarithmic in both axes. Simulated data taken from Ref. [18].

2.10 Correlation coefficients

Once the POVM of the experimental readout process is known, an interesting question is whether the measurements are separable, or whether readout correlations are present. In general readout, it is possible that the state of one qubit affects the readout outcome of another qubit. We categorically emphasize that we do not talk about qubit-qubit entanglement but focus only on phenomena induced by or present in the readout process. A rigorous figure of merit for describing the extent to which the readout of two qubits depend on each other are correlation coefficients [15, 51]. These can be extracted from a two-qubit POVM reconstructed e.g. by detector tomography.

In this thesis we will use classical and quantum correlation coefficients. Former are obtained when only considering non-separability in the computational basis states. In contrast, latter are obtained by considering general superposition states and obtaining the largest possible correlations for any quantum state.

2.11 Readout quality metrics

To validate quantum computers it is important to benchmark the state preparation, qubit control and readout processes. Here, we give a short overview of two important quality metrics used conventionally to quantify the quality of readout for superconducting qubits: assignment fidelity and quantum nondemolitionness.

2.11.1 Assignment fidelity

This metric characterizes the computational basis state distinguishability of a single superconducting qubit [52–54]. To estimate the assignemnt fidelity, an ensemble of both ground and excited states of the qubit are prepared, with the knowledge which state was prepared. This can be performed interleaved (e.g. 0101011010101...), or bunched (0000...0011...111). Due to experimental limitations, in this work the latter method is used. All prepared states are read out with a single shot and compared to the original value. If the prepared value agrees with the measured value, the readout was successful, otherwise it was unsuccessful. Averaging over thousands of prepared computational basis states, we calculate the mean success rate, which we call assignment fidelity.

Assignment fidelity is a metric that is very easily scalable to multiplexed readout and fast to measure and compute. However, it does not take into account possibly correlated outcomes or errors in the readout process. Furthermore, it is not sufficient for fully benchmarking mid-circuit measurements which are often needed for quantum error correction protocols.

2.11.2 Quantum nondemolitionness

The ideal single shot strong readout of a qubit is fully projective. This means that the superposition state of the qubit is projected to one of the computational basis states. The quantum state itself is thus not destroyed. It does not leave the Hilbert space and the system continues behaving according to the rules of quantum mechanics. Such an ideal readout process is called a quantum nondemolition (QND) readout process, as the quantum system stays intact, even though the superposition is lost in a given basis and the state was projected [55–58]. In practice, dispersive readout is not always QND. In some applications, particularly end-of-circuit measurements used in quantum simulations, this is not a problem. However, specifically for mid-circuit measurements QND readout is essential. Examples of performing double readout on a superconducting qubit can be seen in Fig. 2.5

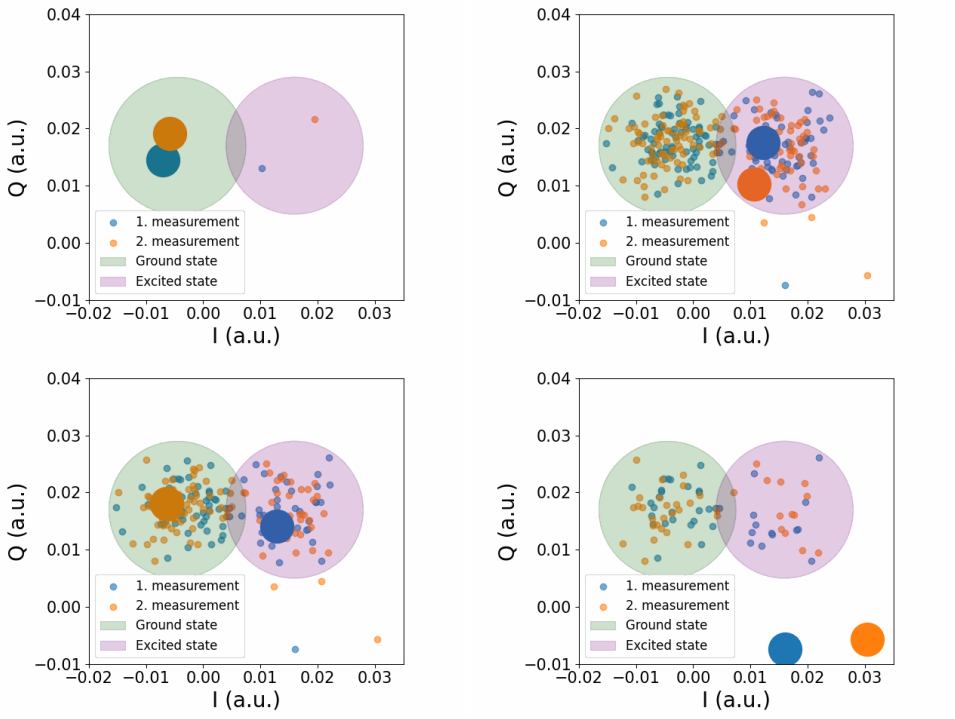

Figure 2.5: Quantum non-demolition readout of a superconducting qubit (a) Both the first and the second measurement place the qubit in the ground state. **(b)** Both the first and the second measurement collapse the qubit to the excited state **(c)** The first and second measurement produce different outcomes. The first measurement was therefore likely not quantum non-demolition and likely altered the qubit states. **(d)** Both the first and the second measurment of the qubit produced a leaked state.

3 Experimental methods

In this section we introduce the most important experimental methods used throughout the thesis. Starting from the cryogenic environment the qubit devices are operated in, we give a detailed background for the microwave manipulation and measurement of the qubits. We explain the crucial differences required for multiplexed readout when scaling up our initial experiments to multiple qubits and show how a qubit system can be tuned up and optimized. Finally, we introduce quantum state tomography also from an experimental perspective.

3.1 Cryogenic environment

Superconducting qubits typically operate at frequencies in the few GHz range [6, 7]. Some exceptions are low-frequency fluxonium qubits [59] and millimetre-wave based architectures [60]. To keep the thermal excitation of the qubit low, the chip needs to be cooled to mK temperatures [6]. Unless mentioned otherwise, all experiments in this thesis are performed below 15 mK, reached by using a commercial BlueFors dry dilution cryostat.

Such a cryostat operates using a mixture of helium-3 (^{3}He) and helium-4 (^{4} He) isotopes, which separate into two phases at temperatures below 0.87 K: a concentrated ^{3}He phase and a dilute phase containing about 6.6% ^{3}He. Cooling occurs in the mixing chamber, where ^{3}He atoms transition from the concentrated to the dilute phase in an endothermic process that absorbs heat, enabling extremely low temperatures [61–63]. Dry cryostats use a pulse tube cryocooler for precooling the ^{3}He gas to approximately 3 K before further cooling stages. The system operates in a closed cycle, with ^{3}He gas continuously pumped, cooled, and returned to the mixing chamber, allowing for automated and sustainable operation without external cryogenic liquids.

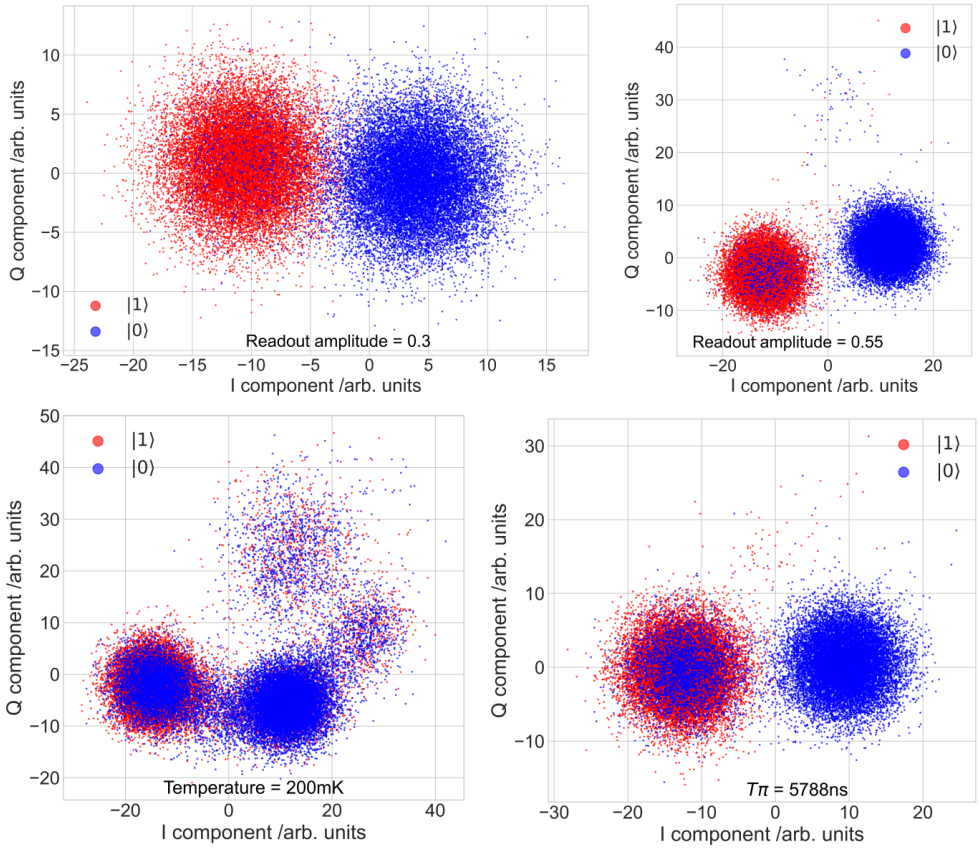

Figure 3.1: In-phase and quadrature (IQ) plane view of single shot qubit measurements. (a) Using too weak readout results in some overlap between the two computational basis states in the IQ plane, lessening distinguishability **(b)** Ideal qubit readout separates the two basis states from each other and does not introduce significant leakage from the two-level system **(c)** Elevated cryostat temperatures result in significant leakage and less distinguishability. The prepared states are very inaccurate, as thermalizing ground state populations does not work well at temperatures $\geq 30\,\mathrm{mK}$ **(d)** Effectively shortened decoherence times lead to decay of the qubit states during single-qubit gates.

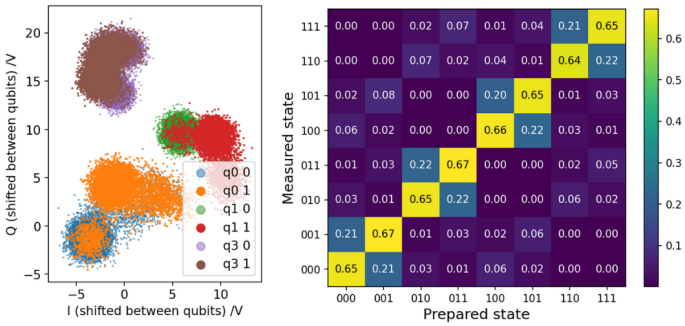

Figure 3.2: Noisy three-qubit multiplexed readout and its confusion matrix Left: Single shot multiplexed readout for three qubits. The two better qubits q0 and q1 have high assignment fidelities but significant leakage to the third excited state. The third qubit, q3, has a very high chance of state misidentification, decreasing the overall assignment fidelity considerably. **Right:** Confusion matrix of the readout. Perfect readout would correspond to an anti-diagonal unit matrix. Due to the combined noise from the readout of all three qubits, the combined computational basis state assignment fidelity is only around 66%.

3.2 Microwave control and readout

The superconducting qubits used in our experiments are manipulated using precisely calibrated microwave pulses that interact with their quantum states [7, 64, 65]. These pulses are generated at room temperature and transmitted to the cryogenic environment of the quantum device via coaxial cables. The microwave signals enable gate operations by resonantly driving transitions between discrete energy levels of the qubit. This interaction is highly sensitive to the amplitude, phase, and frequency of the microwave pulses, which require careful calibration to ensure high-fidelity operations.

For readout, superconducting qubits are typically coupled to microwave resonators [66], although recently alternatives have been developed based on a thermal detector [67] and optical readout [68]. The dispersive coupling shifts the resonator's response depending on whether the qubit is in its ground or excited state, which can be detected by measuring the transmission of a microwave probe signal. Using a Josephson junction array based travellig wave parametric amplifier [69] enhances the signal-to-noise ratio and enables high-fidelity single-shot measurements.

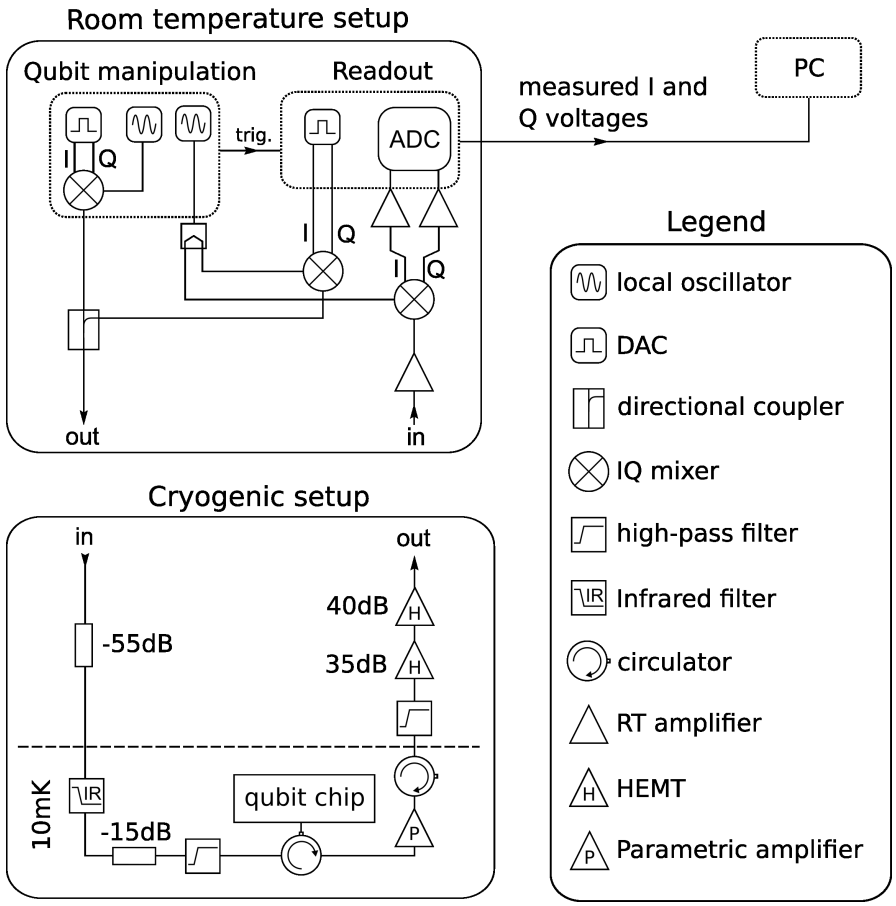

Figure 3.3: Single-qubit microwave measurement setup Microwave frequency pulses are synthesized at room temperature by mixing few hundred MHz pulses with high frequency local oscillator tones. Qubit manipulation and readout pulses are combined with a directional coupler. Signal lines are attenuated on multiple stages for cooling noise levels to the relevant stage. After interacting with the qubit chip, a TWPA and two HEMTs amplify the signal to an order of magnitude of 1 V, which can then be digitized and analyzed again by the time-domain electronics.

3.3 Single-qubit experimental setup

To perform time-resolved experiments with a superconducting qubit, we need to control the qubit state and measure it subsequently. In our setup this is done by two different microwave frequency tones, one which interacts with the qubit to control it, the second with the resonator to measure the qubit. A schematic of the time-domain setup is shown in Fig. 3.3. These pulses are synthesized at room temperature with so-called in-phase quadrature (IQ, or simply quadrature) mixers. Once the two pulses have been generated with appropriate amplitudes, frequencies, phases and lengths, they are combined with a directional coupler which leads the signals into the cryostat. The signal lines are attenuated at every temperature stage to thermalize the room-temperature noise levels. Infrared filters are also used on the last stage, together with microwave filters that get rid of potential side-bands and any other unwanted frequencies that could disturb either qubit or resonator. The signal enters the qubit chip through a circulator, interacts with the resonator, is reflected from the transmission line and enters the circulator again, which now redirects it to the upwards going signal lines. First, the tiny (few photon) signals coming from the resonator are amplified with a near-quantum limited traveling wave parametric amplifier (TWPA), after which further amplification with low-noise high electron mobility transistor (HEMT) amplifiers is necessary. The signal is subsequently integrated sample-by-sample inside a quantum analyzer module with a pulse matching the shape and frequency of the original readout pulse. The resulting complex number is plotted in the complex plane, which we refer to as the in-phase-quadrature plane (IQ plane). Four examples of single shot measurements for different readout parameters are plotted in Fig. 3.1, including weakened readout, ideal readout, readout at higher cryostat temperatures, as well as lengthened readout pulses.

3.4 Multi-qubit experimental setup

To enable quantum control and readout over multiple qubit, it is in principle possible to multiplicate a single-qubit setup and join the individual control and readout signal lines at the chip. However, in practice such methods are very difficult to scale to more than a few qubits. To solve this problem, frequency multiplexing was pioneered [11, 70] and became a widespread method for reading out multiple qubits [17, 54, 71–75]. This technique allows one to combine multiple signals already in the room temperature setup, where significantly less space and heating requirements need to be fulfilled, simplifying the complexity of multi-qubit setups.

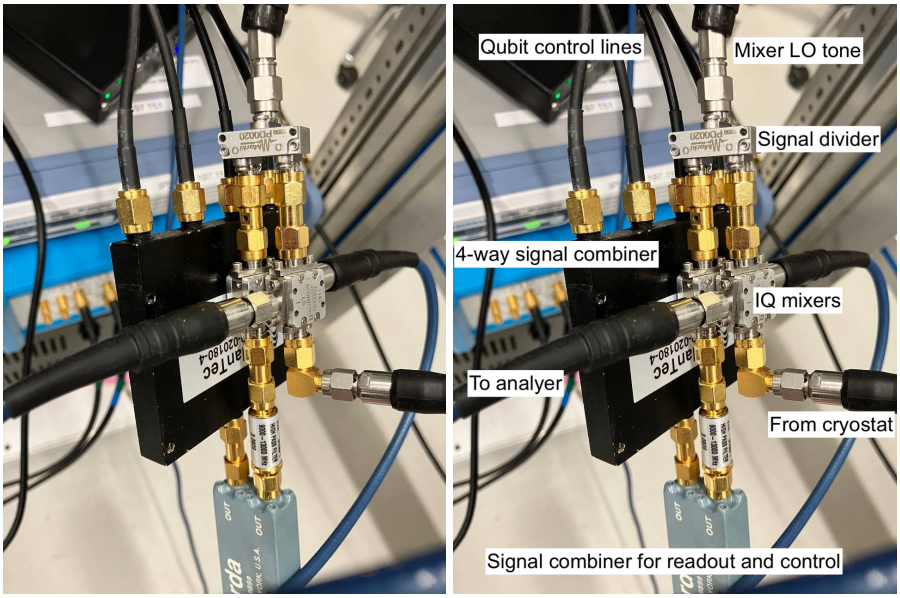

Figure 3.4: Additional room-temperature setup required for operating the multi-qubit device Multiplexed control signal combination is achieved by a 4-way signal combiner. Due to the higher resonator frequencies, additional IQ mixing of the readout signal is needed, which combines the readout pulses with another mixer local oscillator (LO) tone.

A single commercial instrument is able to synthesize both control and readout pulses for on the order of 10 qubits. In our multi-qubit experiments, we combine the control signal outputs from the room temperature time-domain setup with a four-fold microwave signal combiner. To reach the higher resonator frequencies in the multi-qubit chip, an additional room-temperature IQ mixing is required for the readout line. For the additional room-temperature setup, see Fig. 3.4. Apart from this, no major changes are needed to operate our experiments. It is important to note, however, that multiplexed readout can lead to non-negligible crosstalk - the state of one qubit can sometimes affect the measurement outcome of another qubit. These effects are expected to be significant e.g. when two resonators are located next to each other, when their frequencies are close to each other, or when some intermediate mixing frequencies are not sufficiently spaced. Deep neural network-based methods have been recently investigated to decrease crosstalk and increase assignment fidelity [17].

3.5 Experimental readout process

After the above introductions of the general single- and multi-qubit experimental setups used in this thesis, we give a brief overview of the apparatus now exclusively focusing on readout in the context of readout noise.

Once the desired qubit state is prepared with a relevant control pulse, the readout resonator is probed with a pulse, and the resulting signal is analyzed to find out the qubit state. Throughout this thesis, we probe the resonator with its qubit-ground-state frequency, i.e. the frequency which shows the lowest transmission when the qubit is in its ground state. Square and square-Gaussian readout pulses of length $300 - 400\,\text{ns}$ were used. The readout pulse needs to be carefully calibrated so as to not induce unwanted excitations in the qubit (called leakage to higher states), but sufficient photons need to be in the resonator, otherwise the signal-to-noise ration of the measured signal will be too weak. Once the signal is reflected (or transmitted) from the chip, it is amplified by a travelling wave parametric amplifier (TWPA) [69] operated with a pump tone that maximizes single-qubit assignment fidelity. Some signal is lost due to not superconducting cabling. The pump tone is not filtered out perfectly after amplification, resulting in some leakage at a different frequency into the quantum analyzer module. The amplified signal passes through higher-stage amplifiers which add some noisy photons and is integrated in the quantum analyzer module to produce a single, unaveraged point in the microwave in-phase-quadrature component (IQ) plane. Due to multiple mixing stages at room temperature, sidebands are added that might not be filtered out perfectly. A time offset of approx. $300\,\text{ns}$ is introduced between sending the pulse and analyzing the signal to ensure that the pulse had sufficient time to pass through the cabling, chip and other microwave components inside and outside of the cryostat.

3.6 Basic time domain experiments

Here we introduce some of the fundamental time-domain experimental protocols used during tune-up and recalibration of our systems. These are: Rabi and Ramsey experiments used to precisely calibrate single-qubit gates, and single-shot assignment fidelity extraction used to calibrate readout.

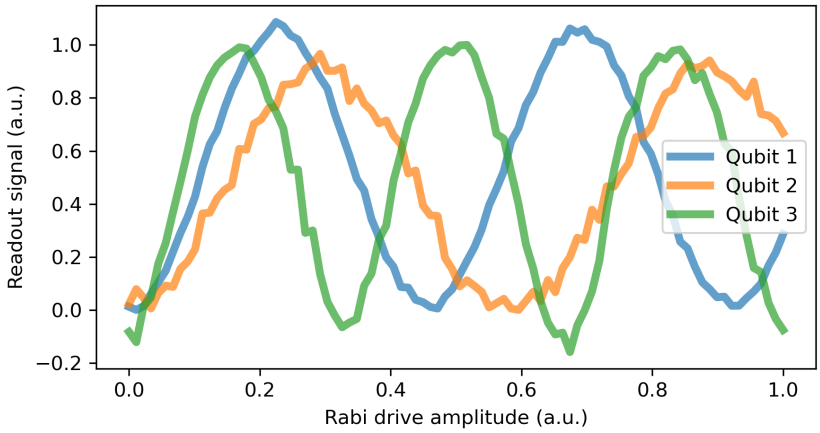

Figure 3.5: Three-qubit multiplexed Rabi experiment The three qubits are driven simultaneously with a power Rabi and measured with a multiplexed readout pulse. The Rabi frequency of the qubits varies and needs to be calibrated individually for performing single-qubit gates.

3.6.1 Rabi experiment

The Rabi experiment serves to identify the pulse needed to drive a qubit from the ground state to the excited state. This pulse corresponds to a π rotation around the X axis of the Bloch sphere, where it also takes its name from: π_X. There are two types of Rabi experiments, one of them consists of sweeping the amplitude, the other one sweeps the length of the driving pulse. Both control pulse sweeps are followed by a readout pulse to obtain the state of the qubit. The pulse sequence for the Rabi experiment is shown in Fig. 3.6 (Rabi).

3.6.2 Ramsey experiment

The Ramsey experiment is performed twice during tune-up to identify the qubit frequency to a few *kHz* precision. The idea behind this technique is to shift the quantum state vector to the equator with a $\pi/2$ rotation, let it precess freely with the frequency difference of the applied pulse and the qubit frequency and rotate it back to a computational basis state with another $\pi/2$ pulse. The resulting signal will exhibit oscillations with the frequency of the detuning between control signals and qubit frequency. The pulse sequence for the Ramsey experiment is shown in Fig. 3.6 (Ramsey).

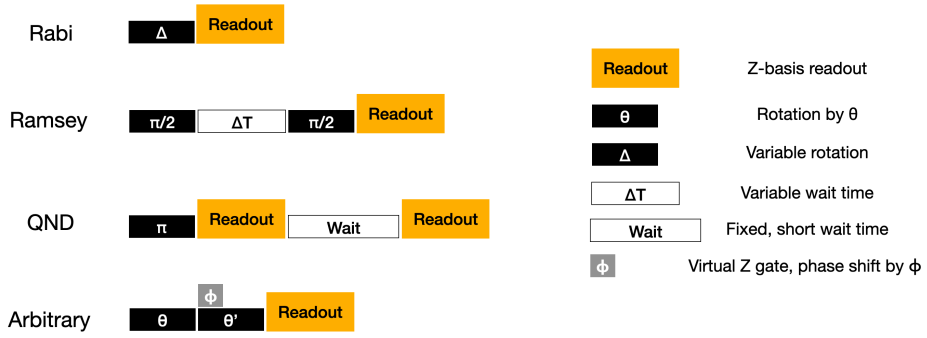

Figure 3.6: Pulse sequences for various time-domain experiments. Rabi- and Ramsey experiments are performed during system tune-up to find the parameters for the single qubit gate π_Z. Quantum nondemolitionness (QNDness) can be estimated by performing two readouts after state preparation. Finally, the pulse sequence for arbitrary basis general quantum state readout is given, as this will be needed for all state- and detector tomography experiments.

3.6.3 Assignment fidelity estimation

There are different ways of assessing the quality of superconducting qubit readout, but by far the most often used one in literature is assignment fidelity. Assignment fidelity can be thought of as the distinguishability of the computational basis states of the qubit after wavefunction collapse (assuming perfect state preparation). To obtain the assignment fidelity of a given readout process, we prepare a total of 10000 ground and excited states and perform classification on them. This can be done either with training on an initial dataset and using the learned rules to predict new datapoints (for the purposes of this thesis, we used K-nearest neighbours) or simply using an unsupervised clustering algorithm on unlabeled data.

3.7 Arbitrary state preparation and readout along different axis

The basis of more sophisticated experiments such as quantum state- and detector tomography (QST and QDT) implemented throughout this thesis is the ability to prepare an arbitrary state on the Bloch sphere and measure it along a different axis. On conventional superconducting qubit platforms the readout is always performed along the Z-axis of the Bloch sphere (by dispersive readout), but by rotating the Bloch sphere itself, the angle of readout can be changed. The pulses used to rotate a state on the Bloch sphere and the Bloch sphere itself are identical and we only

distinguish the two concepts for the ease of understanding. Due to the phase invariance of the Bloch sphere, there is only one azimuthal angle but two polar angles needed to parametrize the experiment. The azimuthal angle corresponding to the phase difference between the axis of readout and the prepared state is implemented by a virtual Z-gate: the phase of the microwave signal corresponding to the rotation of the readout direction is changed. This directly translates to an effective rotation of the Bloch sphere and therefore an adjusted readout axis. The pulse sequence corresponding to arbitrary state preparation and readout along different axis can be found in Fig. 3.6 (arbitrary).

3.8 Bayesian optimization of readout parameters

Quantum devices have figures of merit that characterize their instantaneous operation. In literature, the most often used characterizations include coherence times (T_1 and T_2), single-qubit and two-qubit gate fidelities as estimated from randomized benchmarking, as well as single shot readout assignment fidelities measured on computational basis states. The control parameters of these devices, such as qubit frequency, Rabi drive powers, or readout amplitudes need to be adjusted every few hours to ensure reliable operation. An example of such a device that will be used frequently during this thesis is the traveling wave parametric amplifier (TWPA), which is driven by a continuous microwave tone of given frequency and amplitude. To find the best parameter pair that maximizes assignment fidelity of qubit readout, we use Bayesian optimization based on Gaussian processes. An examplary optimization landscape is plotted in Fig. 3.7. From this plot, we can identify that the amplifier is very sensitive to pump tone settings. Both too low and too high amplitudes and frequencies lead to a rapid loss of signal-to-noise ratio. It is important to note that in this plot, assignment fidelity itself is optimized. Faster optimization could have been performed if only optimizing for the amplitude of the signal, which in some cases was observed to result in significantly higher noise too, overall lowering the signal-to-noise ratio.

3.9 Implementation of quantum state tomography and quantum detector tomography

The goal of quantum state tomography is to reconstruct *the quantum state* before wave function collapse occured. There is some variability in literature in the

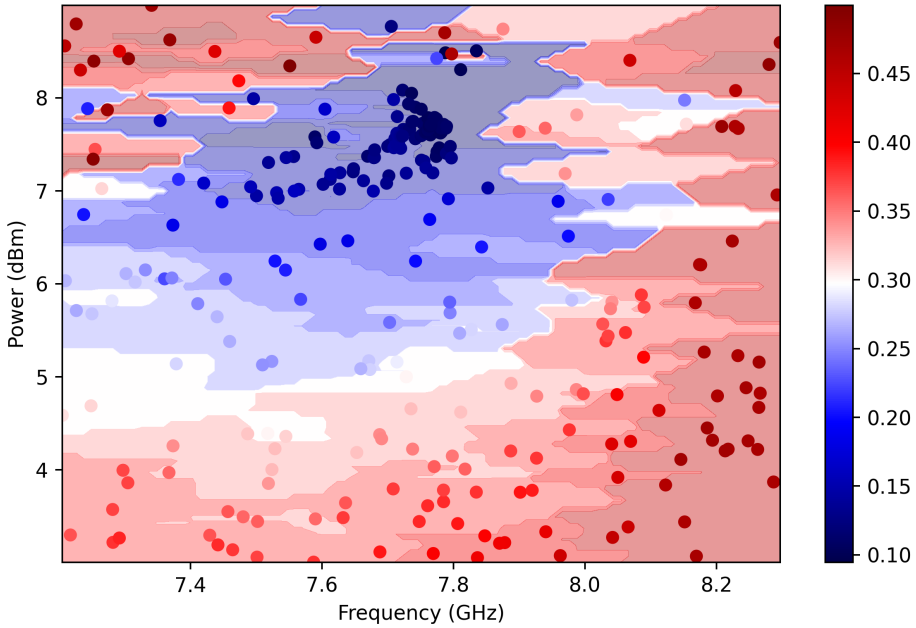

Figure 3.7: Optimizing assignment fidelity as a function of TWPA drive tone parameters (frequency and power) Bayesian optimization based on Gaussian processes is performed to find the highest assignment fidelity. This is achieved by minimizing the readout misidentification rate (i.e. 1-assignment fidelity), plotted in coloured dots. The background is coloured with predictions based on interpolation between measured points. When the misidentification rate is 0.5, the readout produces random values irrespective of the qubit state. A misidentification rate of 0 corresponds to perfect readout. With the best settings for this qubit, the lowest reachable assignment fidelity was approximately 92%.

interpretation of *the quantum state*, in this thesis we will focus on the most general state description, the density matrix of the system.

The underlying assumption of quantum detector tomography is that state preparation is perfect. As this strong assumption cannot be met in any realistic experimental scenario, we will be content with the weaker assumption that state preparation errors are much smaller than readout errors. This condition can be checked by measuring the computational basis state assignment fidelity and comparing it with single qubit gate fidelities. When our experiments are operating at their optimal settings, the measurement inaccuracies are an order of magnitude larger than the single-qubit control operations used in state preparation. When artificially inducing noise in the readout process, the condition is met even more strongly.

To implement quantum state tomography for a single qubit, a given state is prepared and read out along the Z axis. This corresponds to no qubit control rotation

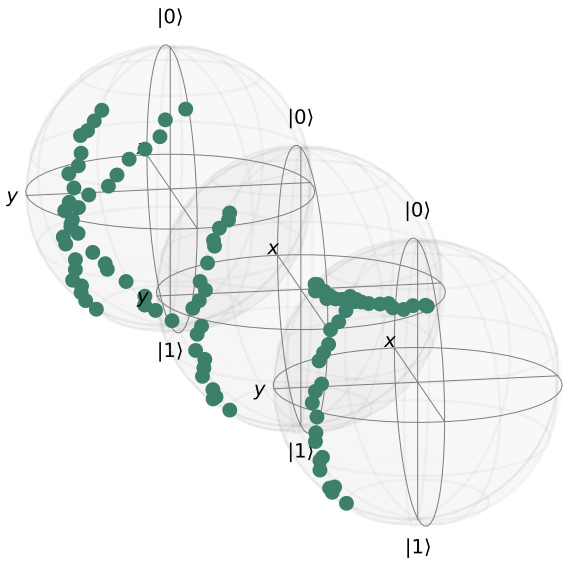

Figure 3.8: Quantum state tomography performed on different states. A given quantum state is prepared on a single qubit, and measured tomographically in the X, Y and Z bases. The results are vector-added to produce a quantum state which can be plotted on the Bloch sphere. The process is repeated dozens of times for different quantum states, which form the letters K, I and T, or KIT for Karlsruhe Institute of Technology. No readout error mitigation was used in the state reconstruction here.

between state preparation and readout. The measurement is repeated a few thousand times to gather statistical data. The process is repeated for X and Y readouts, where a single-qubit control pulse is added between state preparation and readout to effectively transform the Z-basis dispersive shift readout into another basis. Once data from all three projective angles has been acquired, the quantum state can be reconstruced either through simple Cartesian combination in the Hilbert space, or through the use of estimators. A set of unmitigated reconstructed states on the Bloch sphere is plotted in Fig. 3.8.

In contrast, to perform quantum detector tomography for a single qubit, a set of well-defined quantum states is prepared and measured using the detector that needs to be characterized. For each input state, the measurement is repeated thousands of times to collect statistical data on the detector's output. The process is carried out for a complete set of basis states, such as those aligned with the Pauli operators Z, X, and Y, or those aligned with the matrix elements of a symmetric, informationally complete positive operator-valued measure (POVM). To enable

measurements in the X and Y bases, control pulses are applied to rotate the prepared states into the desired basis prior to readout.

After gathering data for all input states, the detector's measurement operator's elements (POVM elements) can be reconstructed. This reconstruction can be performed using techniques like linear inversion or maximum likelihood estimation. The resulting POVM elements provide a detailed description of the detector's functionality.

4 Readout error mitigated quantum state tomography tested on a superconducting qubit

During the calibration of quantum computers, or more generally when performing quantum simulation experiments, it becomes necessary to reconstruct the full density matrix of a qubit. This can prove to be a difficult task even for small system sizes, as the procedure of quantum state tomography generally scales exponentially in terms of qubit number. A second problem is the presence of various noise sources that make the readout process and thus density matrix estimation prone to errors. Recently, a number of methods have been proposed that decrease the effect of readout noise sources on reconstructed quantities [76–78]. A subclass of readout error mitigation based on classical postprocessing is the combination of quantum detector (device) tomography (QDT, sometimes called DT) and quantum state tomography (QST). In such a protocol, QDT serves as a calibration of the measurement process [16], which can be used in the state reconstruction stage [14]. We test the ability of a readout error mitigation protocol in the context of quantum state tomography to counter readout errors. The protocol implemented for our experiments [18] has the special feature that it is capable of taking a more general class of readout errors into account, as conventional methods. A further novelty of the studied approach is the direct connection between the readout error mitigation protocol and the investigated qubit device, allowing full control over the readout process of the device, not normally accessible e.g. on commercial quantum computers. Therefore, we have the ability to directly test the limits of readout error mitigation on a wider variety of noise sources. We artificially induce a range of common noise sources present in superconducting qubit experiments such as decoherence and insufficient readout signal amplification. Quantum infidelity is employed as a measure of accuracy for state reconstruction. To ensure its reliability as a performance metric, the infidelity was averaged over target states sampled uniformly from the Haar measure [79]. An important aspect of the work was to show that some noise sources which directly affect state preparation can stay

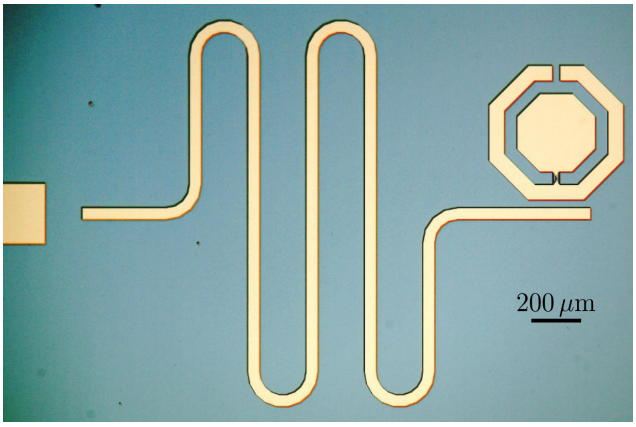

Figure 4.1: Microscope image of the single qubit device The transmission line (left) is coupled to a superconducting resonator (center), which is in turn coupled to the transmon qubit. In this implementation, the qubit has the shape of an octagon. Photo taken from [80].

hidden during readout error mitigation, falsifying the reconstructed density matrix. This observation highlights the need for special attention when using such methods.

4.1 Qubit device

We use a quantum chip with a single transmon qubit coupled capacitively to a readout resonator. A microscope image of the chip can be seen in Fig. 4.1. The chip was fabricated at the National Institute of Standards and Technology (Boulder) by the group of Martin Sandberg and David Pappas. The qubit and resonator frequencies were 6.33 GHz and 8.57 GHz respectively. Qubit control and resonator readout signals are sent down the same signal line. The device is measured in reflection with the help of a cold microwave circulator. The readout signal is amplified directly at the 10 mK stage with a travelling wave parametric amplifier (TWPA). We have direct experimental control over the TWPA's operational parameters, allowing us to dynamically change its amplification strength and thus the computational basis state distinguishability of the qubit.

4.2 Calibration sequence

To perform experiments on the chip, a thorough calibration protocol needed to be performed. This calibration was repeated on a daily basis to counter effects of long-term drifts. The calibration sequence consisted of following parts:

1. **Find resonator frequency**: Using a vector network analyzer (VNA) scan of the transmission line at low power, the frequency of the resonator is identified.
2. **Estimate qubit frequency**: A two-tone measurement was performed which identified the qubit frequency up to a few MHz precision.
3. **Perform Rabi experiment**: A Rabi experiment is performed with a time-domain setup to identify the parameters of a π_X -pulse.
4. **Find exact qubit frequency**: Two Ramsey experiments were performed to calculate the exact frequency of the qubit, up to a precision in the order of 10 kHz.
5. **Find exact π_X gate paramters**: A Rabi experiment was performed with the updated qubit frequency to identify the control parameters for a calibrated π_X gate
6. **Optimization of readout**: Single shot readout is performed 10000 times to find the assignment fidelity of the readout. TWPA and readout pulse parameters are adjusted to reach the highest possible assignment fidelity.

4.3 Running QST and extracting infidelities

Once the chip has been tuned up, we can run the first readout error mitigated quantum state tomography experiment. Quantum detector tomography (QDT) is carried out by preparing each of the six Pauli states and performing measurements in the three Pauli bases, σ_x, σ_y, and σ_z. This process is described by the Pauli-6 POVM. The measurements in the σ_x and σ_y bases are implemented through a combination of qubit rotations followed by a σ_z readout. Quantum state preparation is achieved using virtual Z-gates [81].

Quantum state tomography (QST) is performed by averaging over 25 random quantum states of the form $U|0\rangle$, where U is a Haar random unitary operator [79]. Each of these states is measured in the three Pauli bases. Using Bayesian mean estimation during state estimation has the advantage that the infidelity of the reconstructed state is efficiently calculated on a shot-by-shot basis, without

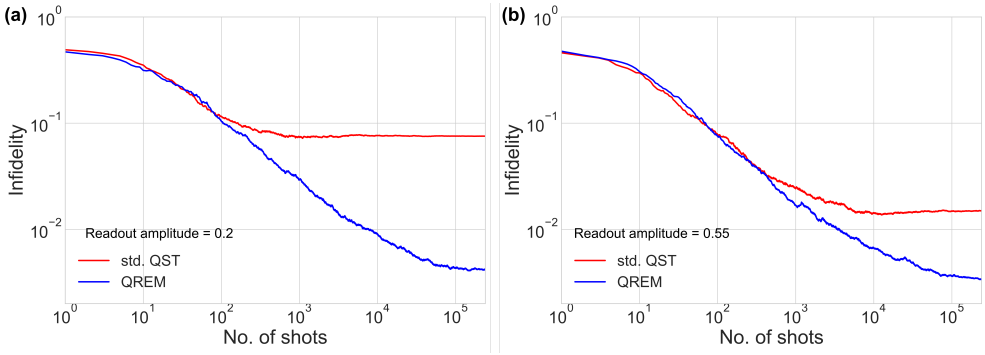

Figure 4.2: Infidelity of quantum state tomography as a function of readout shots with and without readout error mitigation In both plots, x- and y-axes are exponential. In general, infidelity starts decreasing relatively slowly initially. At around 10-100 shots, a linear decrease in the log-log plot is observed, which saturates after a given number of shots. Quantum readout error mitigation aims to lower the infidelity at which state reconstruction saturates. **Left:** If one uses too low readout amplitudes, standard QST fails to reach low infidelities and saturates at around 0.1. Employing detector tomography based readout error mitigation allows over an order of magnitude improvement, and infidelities below 0.01 can be reached. **Right:** With optimal readout settings, readout error mitigation still allows for a significant improvement in state reconstruction.

averaging. This makes it possible to create infidelity vs QST shot diagrams and analyze the behaviour [18]. Here we will focus on the infidelity level which we cannot break below, later used as the "infidelity saturation". The goal of readout error mitigated quantum state tomography is to lower this saturation. An example of performing quantum state tomography with and without readout error mitigation can be seen in Fig. 4.2.

4.4 Inducing noise sources

To study the ability and limitations of the readout error mitigation protocol proposed in [18], different noise sources were induced with varying magnitude. The noise sources can be grouped by their pureness in relation to the readout process: either they manifest strictly during readout, or are present potentially already during state preparation [82, 83].

1. **Pure readout noise:** The induced noise only affects the already prepared state, or the signals coming from the resonators during readout. Pure readout noise arises exclusively during the measurement step, where the quantum state is projected to classical information. This type of noise does not disturb the quantum state prior to measurement but introduces inaccuracies in the

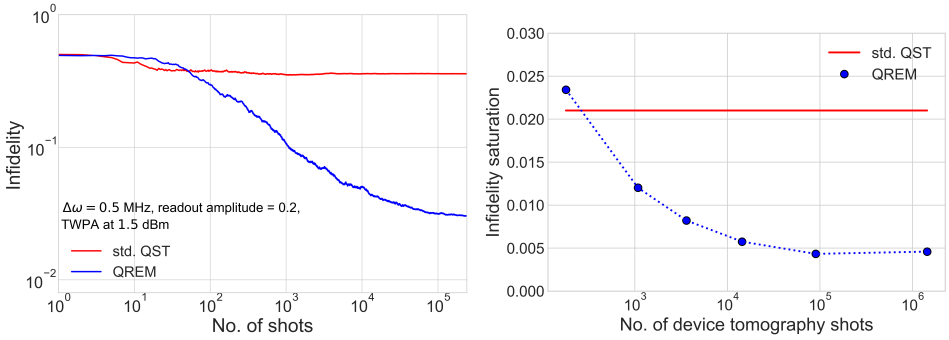

Figure 4.3: Readout error mitigation with mixed readout noises and its dependence on the number of device tomography shots performed Left: General readout error mitigation works well even when multiple noise sources are present. **Right:** Device tomography characterizes the measurement process and is used during the subsequent reconstruction process. Increasing the device tomography shots results in a more accurate model of the measurement operator, enabling higher fidelity quantum state reconstruction. The infidelity saturation cannot be improved beyond a certain level, indicating that the measurement operator is sufficiently characterized

extraction process. The two pure readout noises induced were insufficient amplification and too low/too high readout amplitudes. A further type of pure readout noise would be for instance *readout crosstalk* between two resonators when read out, particularly if their frequencies are close.

2. **Mixed readout noise:** The induced noise affects readout, but also affects state preparation. Such noise manifests both in control and readout and originates from environmental interactions or hardware imperfections that influence the quantum state throughout its lifecycle. For instance, *thermal noise* can disturb qubit states during computation (control and state preparation) and also compromise the quality of measurement. Examples of such not pure readout noise that we study here are effectively shortened coherence times and qubit detuning. A further example could be the effect of magnetic field perturbations that e.g. affect qubit and resonator frequencies. Both studied not pure readout noise sources have the property that they affect the pulses used to prepare the qubit states and the pulses used for the final pre-readout rotation. Control-and-readout noise is more challenging to mitigate compared to pure readout noise, as it requires robust hardware design or real-time error correction mechanisms. Although readout error mitigation protocols can in some instances be of use here, in general a combination of readout error mitigation and quantum error correction may be needed.

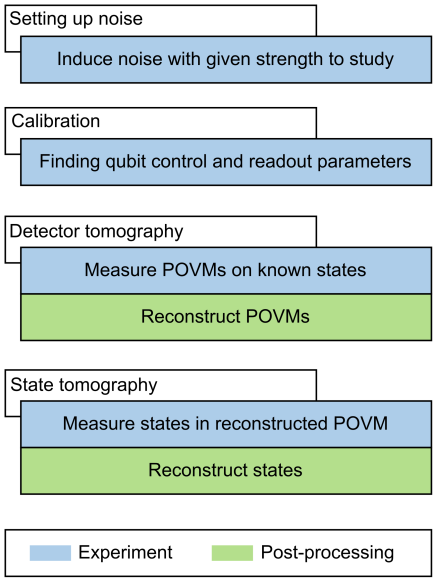

Figure 4.4: Experimental protocol for inducing readout noise and testing the limits of readout error mitigation First, a given noise source is induced and the experiment is recalibrated with the additional noise present. Detector tomography is performed to estimate the noisy POVMs, which are used in the final step, quantum state tomography to enable the reconstruction of the theoretically readout noise-less density matrix.

4.5 Noise resilience of readout error mitigation

In this section we detail our findings of applying the readout error mitigation protocol against different kinds of induced readout noise. As we do not want the infidelities to be limited by an insufficient number of QDT shots performed, we test the dependence of infidelity saturation on the number of detector tomography shots performed and observe a saturation when using at least 10000 shots, see Fig. 4.3 (right). We implement the protocol the way described by Fig. 4.4 where the type and strength of the noise induced in the first step is varied. The infidelity saturation reached after each experimental run is plotted in Fig. 4.5.

Insufficient Readout Amplification

We examine the impact of insufficient signal amplification by the traveling wave parametric amplifier [84] (TWPA - we will call it the amplifier from now on), while

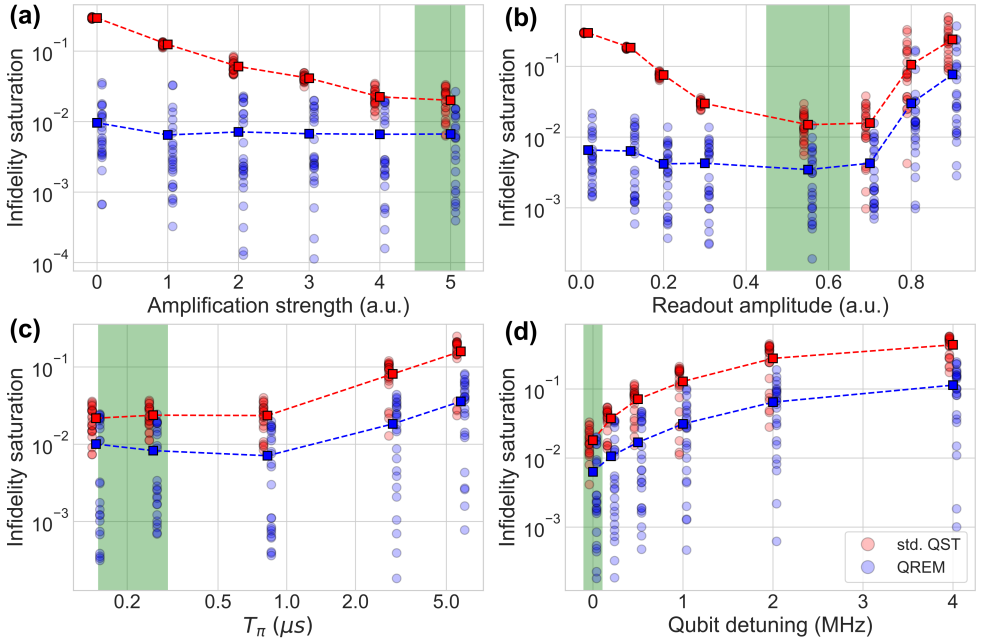

Figure 4.5: Infidelity saturation of readout error mitigated (blue) and standard (red) quantum state tomography for four different noise sources at various strengths The investigated noise sources from top left to bottom right: **(a)** Amplification magnitude of the TWPA: precise state reconstruction is enabled even when the amplifier is turned off (amplification magnitude 0) **(b)** Readout amplitude: low infidelities are achievable even at very low readout powers. At higher powers leakage to higher states becomes dominant. **(c)** Effectively decreased coherence through increased control pulse lengths: readout error mitigation is effective at all pulse lengths but cannot completely mitigate the noise, as this is not a pure readout error. **(d)** Qubit detuning: large improvement seen even for large qubit detuning, but cannot reliably mitigate the effects. This is also due to the fact that this is not a pure readout noise.

ensuring all other amplifiers are operated under optimal settings. The amplification is controlled via the power of the microwave drive applied to the amplifier, which directly affects the distinguishability of computational basis states. This noise is an example of depolarizing noise, effectively shrinking the size of the post-measurement Bloch sphere. Figure 4.5 **(a)** illustrates the measured infidelity saturation values for various amplification levels (in the plot, 0 amplification corresponds to having turned the TWPA completely off, in reality this manifests as an extra attenuation compared to not having a TWPA at all). A reduction in amplification decreases state distinguishability in the IQ plane, leading to high infidelities of approximately 0.3 when the amplifier is completely turned off and readout error mitigation is not used.

Applying the readout error mitigation protocol demonstrates strong resilience against this type of noise. Specifically, reconstruction infidelity remains largely unaffected by this noise source, unless the amplifier is entirely disabled. This indicates that the protocol effectively compensates for the noise introduced by insufficient amplification.

It is important to note that readout error mitigation works on a statistical level, therefore in some applications, particularly for mid-circuit measurements used in quantum error correction, TWPAs are needed and cannot be replaced by implementing readout error mitigation.

Readout Resonator Photon Number

Optimal readout of superconducting qubits requires low resonator photon populations to prevent qubit excitation to higher energy states outside the computational manifold. Low readout power is also needed for non-demolition readout, such as the ones used in active reset protocols. However, an insufficient readout power reduces state separation in the IQ plane, increasing infidelity saturation in state reconstruction. This challenge is successfully handled by the used protocol as shown in Fig. 4.5 **(b)**. In the IQ plane, this noise manifests as a low signal-to-noise ratio similar to what is observed with reduced parametric amplification.

Conversely, higher readout power risks exciting transmon qubits into higher states not accounted for in a two-level system model, resulting in increased infidelities for both mitigated and unmitigated reconstructions. Qubits with large positive anharmonicity such as flux qubits are expected to be inherently more resilient to this noise source.

Notably, unmitigated infidelities exhibit greater variability when readout amplitudes exceed 0.55. This variability likely arises from state-dependent transitions between energy levels (e.g., $0 \rightarrow 2$, $0 \rightarrow 1 \rightarrow 2$, and $1 \rightarrow 2$), which are induced with probabilities dependent on the initial quantum state. At higher readout amplitudes, the ratio between standard QST and QREM infidelities approaches a constant value.

Shortened T_1 and T_2 Times

Decoherence processes are modeled as exponential decay along the z-axis (T_1) and azimuthal directions (T_2) of the Bloch sphere [85, 86]. To study these effects experimentally, we increase manipulation pulse lengths by reducing their power,

thereby allowing more time for energy loss and dephasing. During manipulation, more decoherence effects occur, hence the effective timescale is shortened.

Fig. 4.5 **(c)** shows that longer manipulation durations lead to higher error probabilities due to increased decoherence rates. Both mitigated and unmitigated reconstructions show declining accuracy with increasing pulse lengths, with a consistent factor of 3–4 separating their performance regardless of noise strength. The combined effects of decoherence across all measurement bases are highly state-dependent, explaining the observed variability in infidelity saturation values at fixed noise strengths.

Longer manipulation pulses also induce state decay during preparation stages, classifying this noise source as part of *state preparation and measurement* (SPAM) errors rather than pure readout errors. While restricting decay effects solely to readout could be achieved experimentally by adjusting manipulation power only during readout stages, this approach does not reflect realistic experimental conditions. Instead, uniformly decreasing manipulation power provides a more practical scenario.

Qubit Detuning

Applying frequency-detuned pulses consistently introduces a fourfold reduction in infidelity via our protocol across all detunings (see Fig. 4.5 **(d)**). Interestingly, even small detunings (e.g., 0.1 MHz) yield lower infidelity compared to standard QST under perfect frequency matching. However, QREM's effectiveness diminishes with increasing detuning as infidelity saturation values grow immediately with nonzero detuning.

This limitation comes from inaccuracies introduced during detector tomography due to state preparation errors. As with prolonged manipulation times, one could isolate detuning effects to readout by using resonant pulses for state preparation; however, consistently detuned pulses better reflect realistic experimental scenarios. Therefore this investigated noise source also falls into the category of SPAM errors and is not a pure readout noise.

At 4 MHz detuning, a 200 ns pulse accumulates a phase offset of 0.8, significantly distorting σ_x and σ_y measurement outcomes. Infidelities for both mitigated and standard QST reconstructions increase roughly linearly with detuning before plateauing near 0.5. Variability in measured infidelities comes from strong state-dependent noise effects.

Superconducting qubit experiments can usually be calibrated to significantly less than 1 MHz precision (for example by applying a double Ramsey experiment). Large detunings such as the ones investigated in this section may result from spontaneous iSWAP interactions with neighboring two-level systems (TLS) or microwave source frequency drifts.

While source-induced offsets are generally smaller than considered detunings, TLS-driven frequency jumps exceeding 10 MHz have been observed within timescales comparable to our QST experiments [87]. It is critical that such jumps occur before device tomography; otherwise, reconstructed POVMs will fail to capture these shifts accurately.

For cases where QEM performs suboptimally - e.g., Fig. 4.5 **(c)**, **(d)**, and the high-amplitude regions in **(b)** - the ratio between standard QST and QEM infidelities remains approximately constant. More research is needed to understand this proportionality under increasing noise levels.

Combining Noise Sources

To evaluate the protocol's performance under extreme conditions, we combine multiple strong noise sources: off-resonant driving ($\delta\omega = 0.5\,\mathrm{MHz}$), reduced parametric amplification, and decreased readout amplitude. As shown in Fig. 4.3 (left), conventional QST quickly saturates at high reconstruction errors under these conditions. In contrast, error mitigation enables reconstruction with only a few percent infidelity, demonstrating its robustness even in the presence of very strong readout noise. Reconstruction infidelity scales linearly with shot number on a log-log plot.

4.6 Noise affecting state preparation

We investigate a common experimental noise source for superconducting qubits: the nonzero temperature of the cryostat, which also puts a lower bound on the effective qubit temperature. This in turns leads to significant excited state population in the thermal equilibrium state. Although an important prerequisite of detector tomography based readout error mitigation (namely precise state preparation) is no longer satisfied, one can still execute the experiments and plot the results in Fig. 4.6. This plot must be studied with the knowledge that readout error mitigation requirements are no longer satisfied, as it seems to show low infidelity state reconstruction at temperatures up to 200 mK. These values do not reflect the real infidelity - they are generated in post-processing with strict requirments

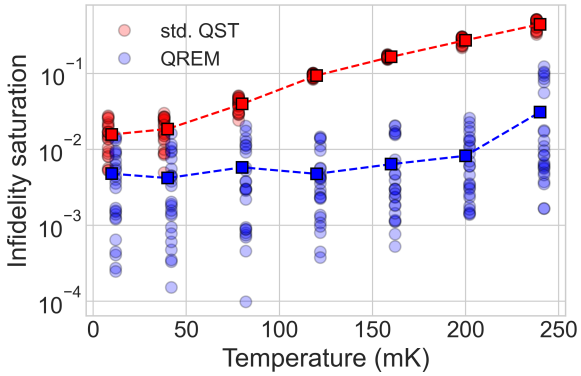

Figure 4.6: Apparent low infidelities at higher cryostat temperatures When measuring at elevated cryostat temperatures, the thermal excited state population is no longer close to zero. This means that state preparation errors are significant. Even though the measured infidelities seem to be very low, state reconstruction is no longer accurate since the conditions needed to use readout error mitigation are no longer given.

that are no longer upheld in the experiment. The real infidelities are potentially $1-3$ orders of magnitude larger. Therefore this plot serves as a warning - readout error mitigation is not a foolproof method, and must always be used with the implications and understanding of the underlying experiment in mind.

4.7 Scaling up

We briefly comment on the scaling properties of the implemented protocol. As any complete quantum state reconstruction method, it is constrained by exponential scaling in both memory requirements and measurement complexity and thus remains feasible for systems with up to 5–6 qubits, particularly if Bayesian mean estimation (BME) [46] is replaced with maximum likelihood estimation (MLE)[48] during state reconstruction. For scaling to such qubit numbers requires fast reset of the qubit, which was not implemented in our experiments. It is clear that larger systems of hundreds, thousands or even more qubits that are becoming commercially increasingly available are not well-suited applications for the protocol in its current state. Recent work focuses on scalability [51, 88], including efficiently breaking down a large system into few-qubit constituents which can be separately readout error mitigated [89].

5 Multiplexed qubit readout metric beyond assignment fidelity

We construct a novel metric for quantifying the information extraction rate from a superconducting multi-qubit chip. The conventional quality metric for readout is assignment fidelity[52–54, 90], which focuses on distinguishing the two computational basis states after wavefunction collapse. Another metric, quantum nondemolitionnes (QNDnes) of readout[91–93] exists to estimate the disturbance of the quantum state induced by the measurement process, making it a suitable and important qualifier for quantum error correction experiments. Here, we investigate a recently proposed metric [19] which can serve as a generalization of assignment fidelity, in a sense that it is averaged over a random distribution of quantum states, instead of only the two computational basis states. This makes it a more complete benchmark of readout quality. We study how the information extraction rate is slowed in the presence of readout noise sources.

We extend the protocol investigated in the previous Chapter to multi-qubit systems. In particular, we investigate two- and three-qubit systems and mitigate their readout errors as a single multi-qubit system. This method is more general than applying readout error mitigation in parallel to all qubits on their own. For example, correlated readout errors can also be mitigated with the more general approach. A possible application is the benchmarking of novel two- and three-qubit entangling gates. Latter have been receiving increased attention lately due to their potentially shorter gate durations and their capability of replacing multiple two-qubit gates. Novel two- and three qubit entangling gates are sometimes not well understood, particularly when discovered by unsupervised reinforcment learning agents. A further important aspect of few-qubit readout error mitigation is its use in scaling up such methods - novel approaches sometimes break up a larger problem efficiently into smaller few-qubit subsets which can then be readout error mitigated more efficiently [89].

We also investigate the existence of readout correlations by extracting quantum- and classical readout correlation coefficients from POVMs reconstructed with detector tomography [15, 51]. Correlated readout errors have recently been observed

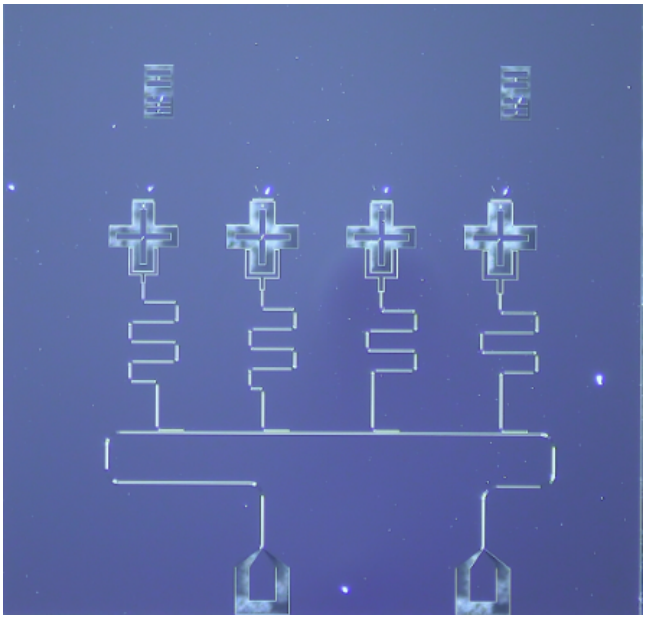

Figure 5.1: The 4-qubit chip used for multi-qubit readout error mitigation and readout correlation experiments Four isolated transmon (Xmon) qubits are each coupled to their individual readout resonator, which are in turned coupled to a transmission line. This transmission line is measured in transmission, with both multiplexed readout and control.

in superconducting circuits with a wide variety of causes [94, 95], for instance mechanical vibrations[96]. Finally, we show that inducing drift in laboratory parameters such as humidity and air temperature through the air conditioner directly affects the reconstructed POVMs corresponding to qubit readout [50].

5.1 Qubit device

The qubit chip used for the experiments in this section consists of four transmon qubits, each coupled to a common transmission line through their individual readout resonators. A microscope image of the chip can be seen in Fig. 5.1. The properties of qubits and resonators are summarized in Table 5.1 and Table 5.2. Coherence times, qubit and resonator frequencies varied slightly between cooldowns, the given values are mean values. High- and low power spectroscopy of the transmission line with the four resonators visible can be seen in Fig. 5.2. The shift in frequency of the individual resonators as a function of power shows that they are coupled to another quantum system, in this case the respective qubits. When mea-

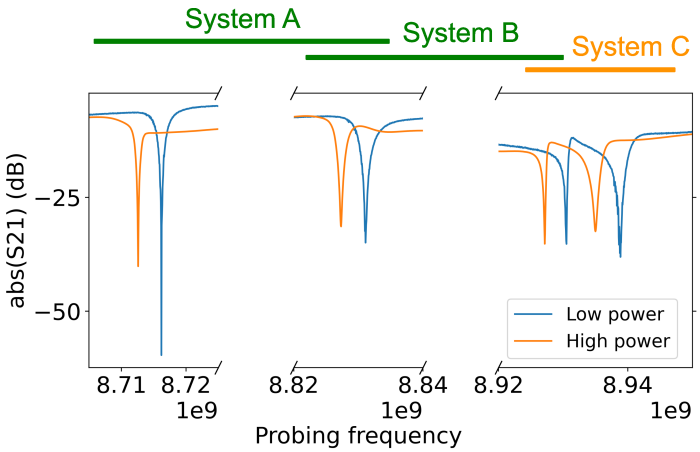

Figure 5.2: Low and high power spectroscopy of the device Four resonators are visible at high powers which shift to higher (System C) have weakly detuned frequencies. The dispersive shift of these resonators enables the time-domain readout of each qubit coupled to its resonator. In this plot, the absolute value of the scattering matrix element S_{21} is plotted.

sured at low powers, the resonators shift depending on the qubit state (*dispersive shift*).

Qubit	ω_{res} (GHz)	ω_{01} (GHz)
q0	8.716	4.455
q1	8.831	5.409
q2	8.931	4.127
q3	8.939	4.926

Table 5.1: Resonator- and qubit frequencies of each of the qubits of the 4-qubit device measured. q0 is the qubit on the physical left side of the chip and they are in ascending order. Qubit and resonator frequencies typically had a variability of around 1 MHz between different cooldowns.

Qubit	Assignment fid.	T_1	T_2
q0	96%	118 μs	67 μs
q1	93%	22 μs	30 μs
q2	92%	27 μs	56 μs
q3	80%	23 μs	ca. 15 μs

Table 5.2: Coherence times and single-shot assignment fidelities of the qubits. The assignment fidelity values show optimized single-qubit readout assignment fidelities. Multiplexed readout fidelities are typically lower.

5.2 Multi-qubit readout error mitigated quantum state tomography

Three-qubit quantum state tomography was conducted both with and without readout error mitigation to evaluate the generalization and scalability of the protocol introduced in Ref. [18] to systems with more qubits. The experiment was repeated on the same prepared quantum state while progressively increasing the number of shots per basis measurement for both detector tomography and state tomography [50]. The results are presented in Fig. 5.3. Infidelities below 0.01 were achieved, with a notable outlier at 12000 shots per basis measurement, likely caused by measurement drift. A comparison between the theoretically expected density matrix and the reconstructed one, both with and without readout error mitigation, is shown in Fig. 5.4.

We observe an improvement in infidelity by approximately a factor of 30 when comparing state tomography results with and without readout error mitigation. This demonstrates that the method introduced in Ref. [18] is scalable to three superconducting qubits and is successful at mitigating readout errors. Consequently, this approach provides a pathway to benchmark and analyze three-qubit gates, even in the presence of coherent readout errors. This is particularly relevant given the renewed interest in three-qubit gates within the community [97–99], due to their potential for higher fidelity, shorter gate durations, and ability to replace multiple two-qubit gates.

5.3 Infidelity convergence thresholding

We briefly motivate the necessity of readout error mitigation for determining the crossing of infidelity thresholds in our two-qubit experiment. Fig. 5.5 displays six mean infidelity curves: three readout error mitigated (QREM, blue) and three unmitigated (std. QST, red), plotted as a function of the number of shots used for state tomography. Each curve represents an average over 16 products of single-qubit Haar random states [79]. The crossing points of these curves with specific constant infidelity values (0.2, 0.15, and 0.1) are determined using a Bayesian mean estimator [18]. This approach enables precise identification of the shot number at which the infidelity curve intersects a given threshold.

We observe that the unmitigated curves saturate at high infidelity values and, under significant noise levels, fail to cross these thresholds (indicated by green horizontal lines). These thresholds correspond to those used in Fig. 5.6 and Fig. 5.7,

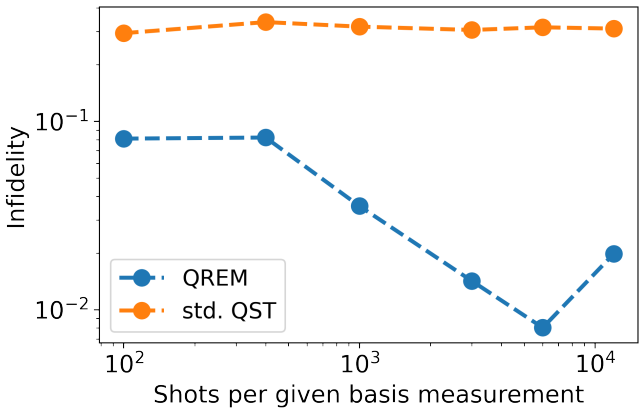

Figure 5.3: Infidelity evolution of 3-qubit multiplexed quantum state tomography as a function of shots performed Over an order of magnitude improvement in infidelity is observed for the single quantum state reconstructed here. The readout error mitigated infidelity curve (blue) has a noticeable bump at the end, where the infidelity seems to grow again. This is attributed to drift, as the time needed for such precision is multiple hours.

rendering unmitigated curves unsuitable for accurately benchmarking readout quality. In contrast, the readout error mitigated infidelity curves (blue) cross the thresholds within the steady exponent domain (i.e., the linear region of the log-log plot), making them more reliable for benchmarking purposes.

Additionally, we find that Bayesian mean estimators provide more accurate infidelity curves compared to maximum likelihood estimators during reconstruction. While Bayesian mean estimators are computationally efficient for two qubits, maximum likelihood estimators offer an additional advantage in speed for larger systems.

5.4 Readout noise and its impact on information extraction rate

We conduct readout error mitigated two-qubit quantum state tomography experiments on System A (see Fig. 5.2) to study how readout noise affects the rate of quantum information extraction from the system. This is of particular interest, as the quantum-classical boundary must be crossed once a general quantum computation is finished and the quantum information needs to be converted to information which a conventional classical computer, or person can handle. While assignment

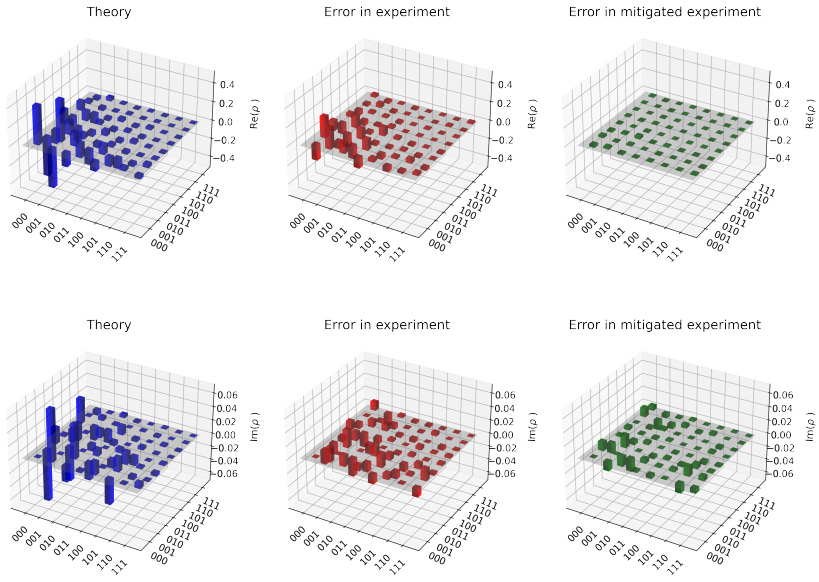

Figure 5.4: Three-qubit quantum state tomography, real and imaginary parts. Left: Real and imaginary parts of the pure quantum state prepared in the experiment. **Middle:** Errors in the density matrix of the reconstructed three-qubit density matrix without using readout error mitigation. Multiplexed readout induces significant readout errors that bias the reconstructed density matrix. **Right:** Errors in the reconstructed density matrix after readout error mitigation has been applied in post-processing. Both real and imaginary parts of the density matrix are now significantly closer to the theoretically expected values.

fidelity is commonly used to evaluate readout quality in superconducting qubits, it does not fully capture the rate of information extraction, as it only considers computational basis states.

5.4.1 Varying readout power

We simultaneously vary the readout power for both resonators, ensuring they remain equal at all times. This creates - at least in principle - a potential for multiple optima in the information extraction rate. In Fig. 5.6 **Left**, the number of shots required to achieve specific infidelity thresholds is plotted. The results reveal a single optimum for information extraction at a readout amplitude of 0.48 (a.u.).

This finding aligns with both the product and sum of single-qubit assignment fidelities, as shown in Fig. 5.6 **Right**. While the optimum identified in Fig. 5.6 **Left** is statistically significant, the assignment fidelities exhibit a plateau between

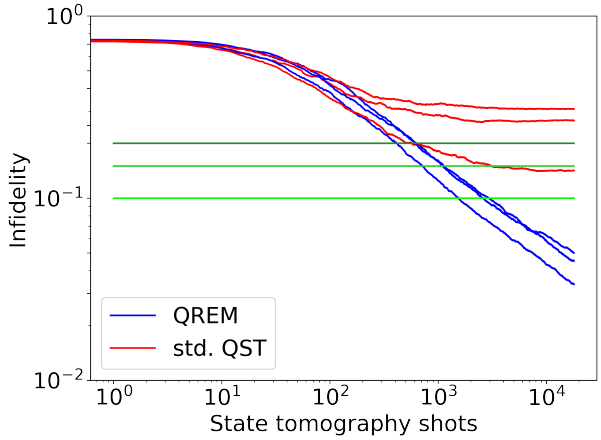

Figure 5.5: Infidelity threshold based readout precision metric for a two-qubit system Quantum readout error mitigated quantum state tomography is performed for three different noises, the resulting infidelity curves are plotted in blue. We indicate specific infidelity levels (green horizontal lines) and check where the readout error mitigated infidelity curves cross. The resulting number of shots can be used as a metric to quantify the rate of information extraction from the system.

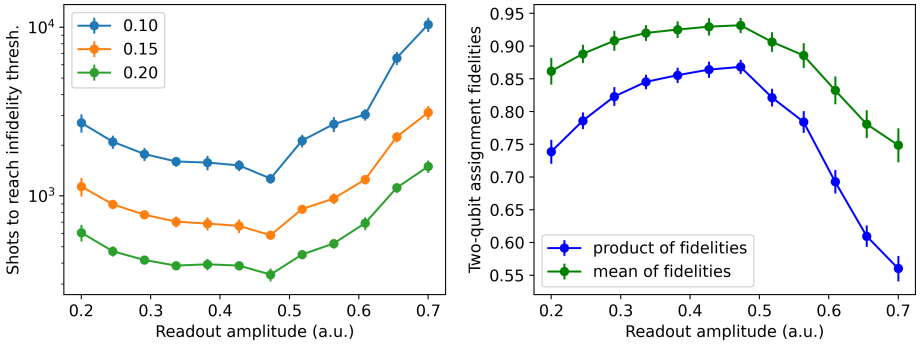

Figure 5.6: Shots to reach given infidelities in readout error mitigated quantum state tomography and corresponding assignment fidelities as a function of readout amplitude. Left: Infidelity based benchmarking shows that the ideal operating parameter for maximizing the rate of information extraction from the two-qubit system is at approx. 0.48 a.u. **Right:** Sum and product of assignment fidelities for the two qubits as a function of readout amplitudes. The two methods for evaluating the quality of multiplexed readout show good agreement about the ideal readout amplitude.

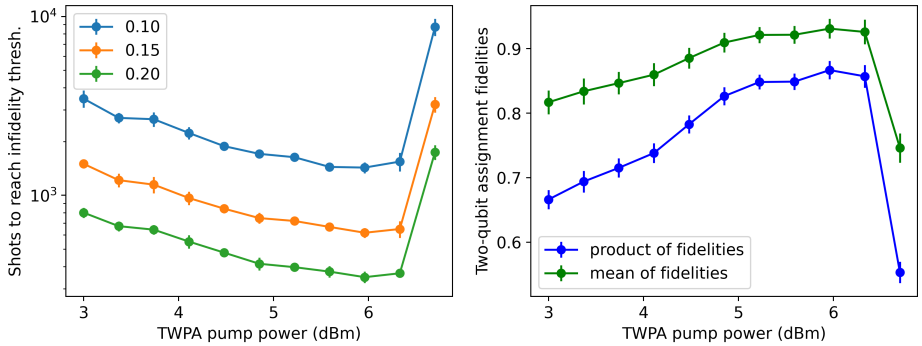

Figure 5.7: Shots to reach given infidelities in readout error mitigated quantum state tomography and corresponding assignment fidelities as a function of readout amplitude. Left: Infidelity based benchmarking shows that the ideal operating parameter for maximizing the rate of information extraction from the two-qubit system is at $\approx 5.98\,\mathrm{dBm}$ **Right:** The two methods for evaluating the quality of multiplexed readout show good agreement about the ideal TWPA pump power.

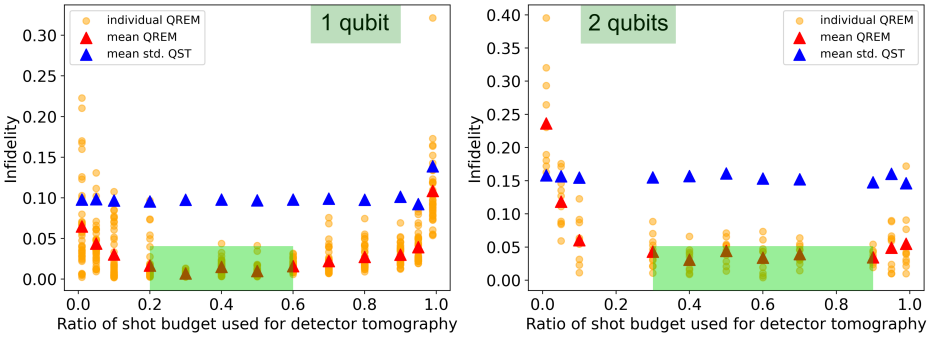

Figure 5.8: Infidelity of quantum state reconstruction for a given shot budget ratio used for detector tomography for single- and two-qubit experiments. Left: Infidelity reached when allocating a set shot budget to detector tomography. If the ratio is too low, the noisy measurement operator is not estimated well, if the ratio is too high, quantum state tomography does not reach the infidelity saturation level. **Right:** Infidelity of two-qubit quantum state tomography experiments. The ideal shot ratio for reaching the lowest infidelity is higher than for single-qubit experiments. The green bars on the x-axes of both plots highlight the identified optimal ratios of the shot budget.

readout amplitudes of 0.35 and 0.48, due to relatively large error bars caused by the limited number of computational basis states measured. Repeating these experiments with more shots is expected to further highlight a clear optimum at 0.48 (a.u.) readout power.

The overall features of the readout parameter landscape can be attributed to low state distinguishability at lower readout powers and state leakage at higher powers, consistent with observations in Ref. [90]. Both the assignment fidelity and infidelity convergence landscapes are in accordance with this reasoning.

In summary, for this experiment, the sum and product of assignment fidelities proved to be reliable indicators of how quickly information can be extracted from separable states within the two-qubit manifold. Both methods agree on the existence and location of a single optimum for optimal two-qubit multiplexed readout.

5.4.2 Parametric amplification

The resonators in System A are detuned by approximately 115 MHz from one another, leading to different optimal operating parameters for the shared TWPA due to its nontrivial frequency-dependent gain profile, as described e.g. in Ref. [69]. Consequently, testing the TWPA on a single qubit is insufficient. Performing state tomography on this system (see Fig. 5.7), we observe that information extraction is fastest at a room-temperature stage pump power of approximately 6.3 dBm. This corresponds well with the maximum of both the sum and product of single-shot assignment fidelities.

When the TWPA is oversaturated with pump power, information extraction slows significantly—by about a factor of 6 compared to the optimum. At low pump powers, reduced distinguishability between computational basis states during readout also slows down information extraction, as reflected in corresponding assignment fidelities.

These results demonstrate that infidelities derived from readout error mitigated quantum state tomography can serve as a valuable tool for assessing multiplexed qubit readout quality, going beyond the limitations of assignment fidelity measures, which are experimentally less demanding but more restricted. For comprehensive benchmarking and certification of quantum computer readout performance, we recommend using both methods.

5.5 Shot budgeting between quantum detector- and state tomography

In experiments, the runtime is often constrained due to factors such as experimental drift or the need to share resources. This limitation raises the question of how to optimally distribute a fixed measurement budget between detector tomography and state tomography to minimize the resulting infidelity in the reconstruction of a quantum state.

We define the shot ratio as:

$$r = \frac{\text{QDT shots}}{\text{QDT shots} + \text{QST shots}} \tag{5.1}$$

where r represents the fraction of total shots allocated to quantum detector tomography (QDT) relative to the total number of shots used for both QDT and quantum state tomography (QST).

To determine the optimal ratio for our experiment, we conducted single- and two-qubit tomography while maintaining a fixed total number of shots for various values of r. For single-qubit reconstruction, we ensured representative convergence of state reconstruction by averaging over the same 40 Haar random states for each value of r. For two-qubit shot budgeting, we used 10 products of single-qubit Haar random states.

The experimental results are presented in Fig. 5.8. For both single- and two-qubit readout error-mitigated state tomography, allocating half of the shot budget to calibration (QDT) is a reasonable choice. When very few shots are allocated to calibration, the resulting infidelity is constrained by sample fluctuations in the estimated measurement operator. Conversely, when too few shots are allocated to state tomography, the experiment cannot achieve the lowest possible infidelities. The optimal ranges for the shot ratio are highlighted in green in Fig. 5.8. From these plots, we estimate the optimal value of r, as defined in Eq. (5.1), to be:

$$r_1 = 0.4 \pm 0.2$$

for single-qubit experiments and:

$$r_2 = 0.6 \pm 0.3$$

for two-qubit experiments.

5.6 Readout correlation coefficients in two-qubit systems

We perform detector tomography on Systems A and C (see Fig. 5.2) to extract quantum and classical correlation coefficients as functions of the number of detector tomography shots. The results are shown in Fig. 5.9. At low shot numbers, the correlations are primarily influenced by sample fluctuations in the reconstructed POVM, which diminish as the number of shots increases. Therefore, these values serve only as upper bounds on the correlations until they saturate with increasing detector tomography shots.

While saturation is not observed in System A, it is clearly evident in System C. This difference is attributed to the frequency spacing of the resonators in the two systems: $\delta_A = 100\,\mathrm{MHz}$ compared to $\delta_C = 8\,\mathrm{MHz}$.

Detector tomography thus provides a precise tool for probing correlations beyond those arising from the measurement basis, enabling an assessment of whether resonators are sufficiently separated both spatially on the chip and in the frequency domain. Since correlations depend on in-situ readout variables such as readout power, it is possible to optimize these parameters to maximize the rate of information extraction while minimizing correlations between different qubit readouts. These results pave the way for a more comprehensive optimization of multi-qubit readout systems.

5.7 Readout correlation coefficient dependence on readout noise

The dependence of readout correlations on the presence of a readout noise source was investigated by reducing the distinguishability of computational basis states through the use of readout pulses with varying amplitudes. The relative readout amplitude is defined as the ratio between the applied amplitude of the readout tone and its ideal amplitude. To prevent leakage into higher energy levels, the study was limited to reduced readout amplitudes, corresponding to relative readout amplitudes not exceeding 1. At the extreme, the single-shot assignment fidelity measured with a relative readout amplitude of 0.1 is approximately 55%, compared to about 95% at a relative readout amplitude of 1.

The experimental results, presented in Fig. 5.10, demonstrate that, within the experimental bounds, both quantum and classical correlations remain unaffected

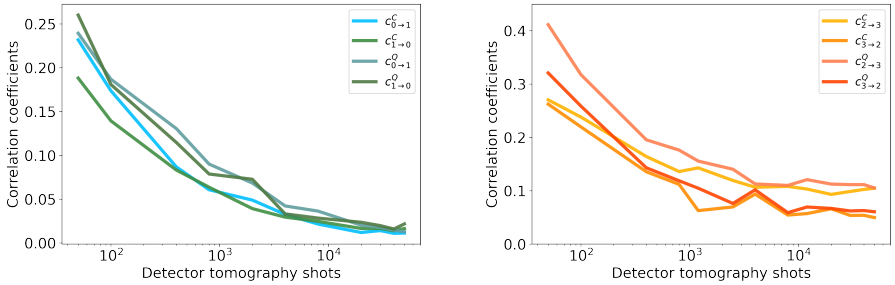

Figure 5.9: Classical and quantum correlation coefficients for two different two-qubit systems as a function of detector tomography shots. Left: All quantum and classical correlation coefficients extracted from the two-qubit measurement operators tend to zero within the limits of the experiment as the number of detector tomography is increased. There are no significant correlations present in the POVMs. **Right:** Both quantum and classical correlation coefficients tend to a constant nonzero value as the number of detector tomography shots is increased. The correlations do not have significant directionality but quantum readout correlation coefficients are larger than classical readout correlation coefficients.

by the strength of the readout noise, even under conditions of very high noise levels.

5.8 POVM dependence on induced experimental drift

Quantum computers are intricate systems whose performance depends on a large number of factors. Under laboratory conditions, many of these factors can be kept under control within some precision e.g. by using dilution refrigerators, magnetic shielding, placing the lab undeground, far away from train lines etc. Unfortunately, not all external factors can be controlled sufficiently, therefore the quantum system will be disturbed occasionally. Quantum error correction protocols are currently being developed to counter such unforeseen, potentially random events that can destroy a quantum computation in progress.

Here, we investigate how external effects, in particular the combination of continuous humidity and temperature changes influence the effective measurement operator. Since the runtime of both quantum detector and state tomography increases exponentially with the number of qubits, experiments must be conducted self-consistently over extended periods.

However, the duration of such experiments is constrained by temporal drifts in operational parameters. To quantitatively assess the timescales and impact of these

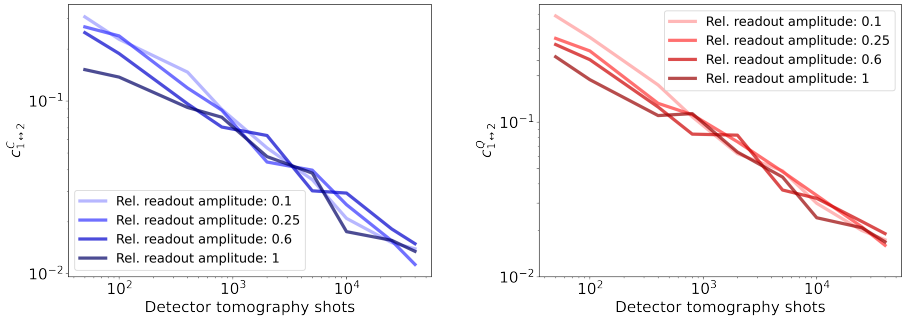

Figure 5.10: Independence of readout correlation coefficients from readout noise Left: Symmetric classical readout correlation coefficients are independent of the readout amplitude used. The relative readout amplitude (rel. readout amplitude) is the amplitude relative to the best setting. Even at 1% of the optimal readout power, correlation coefficients are the same within experimental bounds as with optimal readout, although the computational basis state distinguishability is heavily impacted. **Right:** Quantum correlation coefficients are also independent of the relative readout amplitude, and therefore independent of induced readout noise.

drifts on our POVMs, we performed repeated two-qubit detector tomography over 11 hours while monitoring the laboratory's temperature and humidity.

Specifically, we reconstructed the measurement operators for ZZ and XX basis multiplexed readout of System A and plotted their coherent errors in Fig. 5.11. The coherent errors in the ZZ basis were small and could be attributed to statistical fluctuations, whereas significant coherent errors were observed in the XX basis. This discrepancy is explained by the additional rotation gates required for XX basis readout, which are not needed for ZZ basis measurements. Under stable laboratory conditions, the errors remained temporally consistent for both bases. However, when rapid changes in temperature and humidity were introduced by disabling the laboratory air conditioning, a significant drift in coherence was observed in the reconstructed measurement operator for the XX basis. In contrast, the ZZ basis coherences remained stable. This suggests that the source of coherence drift is likely associated with qubit manipulation used in XX basis measurements. We note that the intrinsic properties such as coherence times or frequencies of the superconducting device are not likely influenced by the outside changes in temperature. The cryostat temperature at the 10 mK stage was continously tracked and no significant heating effects over 1 mK were observed. Instead, the coherent errors likely came from temperature-dependent attenuative or reflective properties of the room temperature cabling, or humidity sensitive local oscillator output power, for example.

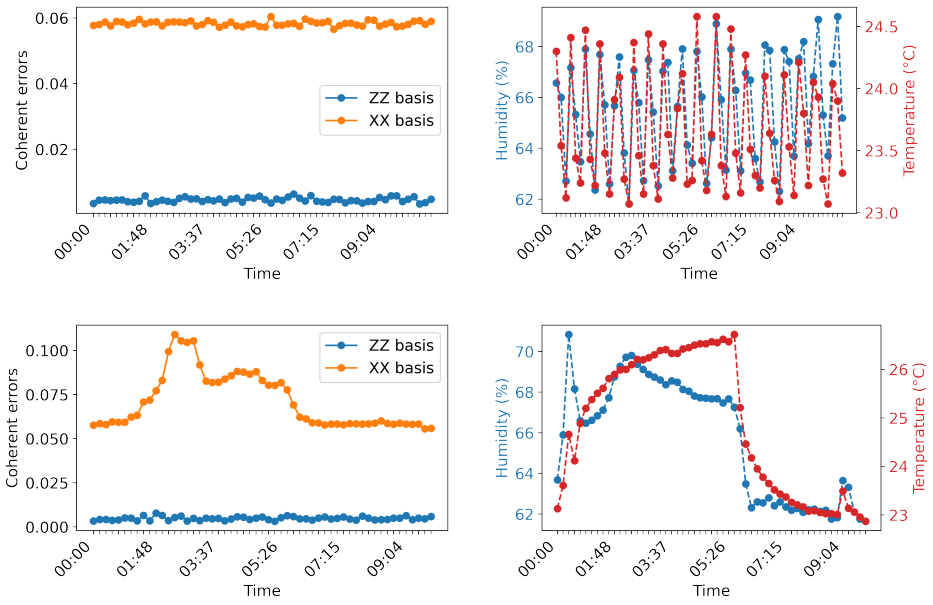

Figure 5.11: Coherent readout errors are unstable when laboratory parameters such as temperature and humidity change Top row: When the air conditioning unit is running continuously, temperature and humidity are temporally stable and no significant changes in coherent readout errors are observed either in the ZZ, nor in the XX readout bases. **Bottom row:** Turning off or on the air conditioning unit induces significant coherent errors in the XX basis, but not in the ZZ basis. This is likely due to the control pulses applied during XX two-qubit readout.

6 Correlation-conscious optimization of multiplexed qubit readout

Efficient and accurate qubit readout is a critical component of scalable superconducting quantum processors. Multiplexed readout [11], where multiple resonator-qubit systems share a single transmission line, offers a practical solution to the hardware overhead associated with traditional single-line readout schemes. However, this approach introduces challenges such as crosstalk [15, 51, 100] between resonators, which can degrade readout fidelity and introduce unwanted correlations between measured signals. These effects become particularly pronounced when resonators are closely spaced in frequency, potentially leading to overlapping dispersive shifts and complex signal dependencies.

We investigate a two-qubit subsystem on a four transmon qubit chip. This subsystem has resonators that are only spaced by 8 MHz and exhibits strong readout crosstalk. For more information about the used chip, see [19]. Performing multiplexed Rabi experiments shows that the signals observed on the two resonators are not independent from each other. A signal applied to one of the qubits can also be measured on the neighbouring resonator. We show that this phenomenon strongly depends on the readout parameters used.

The conventional readout quality metric, assignment fidelity [52–54, 101, 102], also depends strongly on readout parameters. This means that one cannot independently optimize for high assignment fidelity and low crosstalk. To address this, we develop a correlation-conscious optimization strategy that incorporates both assignment fidelity and quantum correlation coefficients into a unified figure of merit. Using Bayesian optimization [103], we demonstrate that it is possible to suppress readout correlations by up to a factor of two without significantly compromising readout assignment fidelity.

Our results highlight the importance of considering both fidelity and correlation metrics when designing multiplexed readout schemes for larger-scale quantum systems. This work provides a pathway for improving the reliability of qubit measurements in superconducting quantum processors.

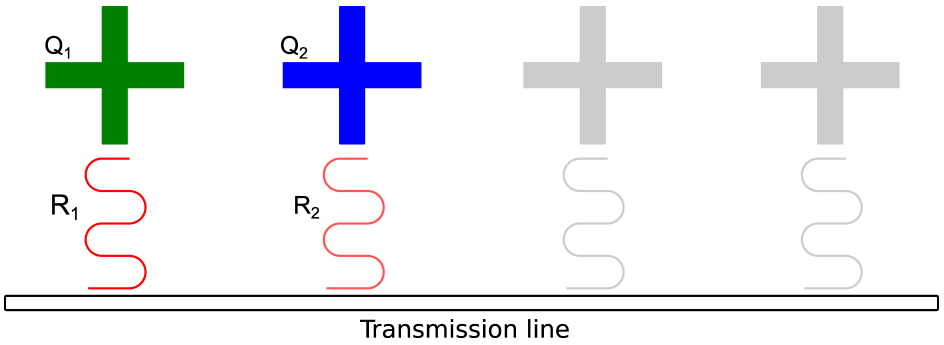

Figure 6.1: Layout of the system used to investigate readout correlations R1 and R2 are the resonators coupled to Q1 and Q2. R1 and R2 are only detuned in frequency by approx. 8 MHz. The two other qubits and resonators (marked in grey) are not controlled and read out during the experiments in this Chapter.

6.1 Qubit device

The qubit device used for the investigation of correlation-conscious optimization of multiplexed qubit readout is identical to the device used in Chapter 5. In particular, we focus on the two neighbouring resonators with the highest frequencies (r_2 and r_3 in Fig. 5.2), which we will now call R_1 and R_2. The naming convention for this chapter can be found in the schematic Fig. 6.1. An important property for this two-qubit subsystem is their weak frequency detuning: $\omega_{r_3} - \omega_{r_2} \approx 8\,\text{MHz}$ placing it into the same order of magnitude as the dispersive shift.

6.2 Observation of strong, readout parameter-dependent crosstalk

We perform a Rabi experiment on one qubit while reading out both qubits. From the resulting oscillations, we extract the signal-to-noise-ratio (SNR) for each resonator. A non-zero SNR in the resonator not coupled to the driven qubit is interpreted as crosstalk.

In Fig. 6.2, both resonators exhibit Rabi oscillations with matching frequencies, even though only Q_2 was driven. This indicates a correlation between the readout of the two qubits.

We use a quantitative method to estimate correlations in measured signals by fitting a sinusoidal function to the datasets from both resonators and calculate the

remaining residuals from these fits. This allows us to directly extract SNRs for the oscillations. In such a constellation, the residuals are the noise, the amplitude of the fitted sine function is the signal. A high SNR (with values well above 1) corresponds to a well-defined signal. Under ideal readout conditions, where the signals from the two resonators are uncorrelated, this experiment would yield a high SNR for R_1 and an SNR close to zero for R_2.

To investigate the readout parameter dependence of the observed crosstalk, we systematically vary the readout amplitudes for each measurement pulse and plot the SNRs for both resonators in Fig. 6.3 **(a)** and **(b)**. The plots reveal regions with varying levels of crosstalk and differing SNRs for the resonator coupled to the driven qubit. In Fig. 6.3 **(a)**, where only Q_1 is driven, increasing the readout amplitude for R_1 improves the SNR but also increases correlations with R_2. When R_2 is driven at approximately 0.3 (a.u.), a significant drop in Q_1's SNR occurs, accompanied by strong correlations. This region of high crosstalk expands as the amplitude of R_1 increases.

In Fig. 6.3 **(b)**, where only Q_2 is driven, we identify an optimal readout region when R_2 (vertical axis) is between 0.15 and 0.35. However, this region is disrupted by two branches of SNR loss, which also induce strong correlations in R_1. These branches originate from $R_2 \approx 0.26$ (a.u.) and split into two as the amplitude of R_2 increases. For high-quality independent qubit readout, it is necessary to select regions where the SNR of the corresponding resonator is high and correlations with the neighboring resonator are minimal.

To explore the source of this readout crosstalk, we performed multiplexed readout of both resonators without driving any qubits. This test examines whether the resonators deform or shift when driven. If their shapes remained unchanged, the measured signals in Fig. 6.3 **(c)** would vary linearly with R_1 or R_2, independent of the other variable. However, this behavior was not observed. Instead, the measured patterns closely resemble the regions of high correlations identified earlier. This suggests that the nontrivial dependence of readout correlations arises from nonlinear behavior in the resonators when driven off-resonance.

6.3 Correlation-conscious readout metric

The observation of readout crosstalk in the computational basis states highlights the necessity of fully characterizing the correlations induced by readout. Such characterization enables the mitigation of these correlations through appropriate selection of readout parameters.

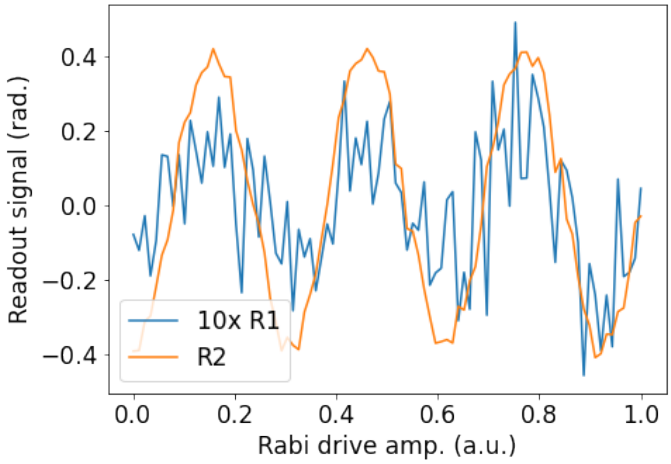

Figure 6.2: Readout crosstalk in a multiplexed Rabi experiment Rabi oscillations are driven on qubit 1, but both resonator 1 (R1) and 2 (R2) are read out. The Rabi oscillation appears in the signal coming from both resonators, but is much more pronounced on the resonator coupled to the drive qubit.

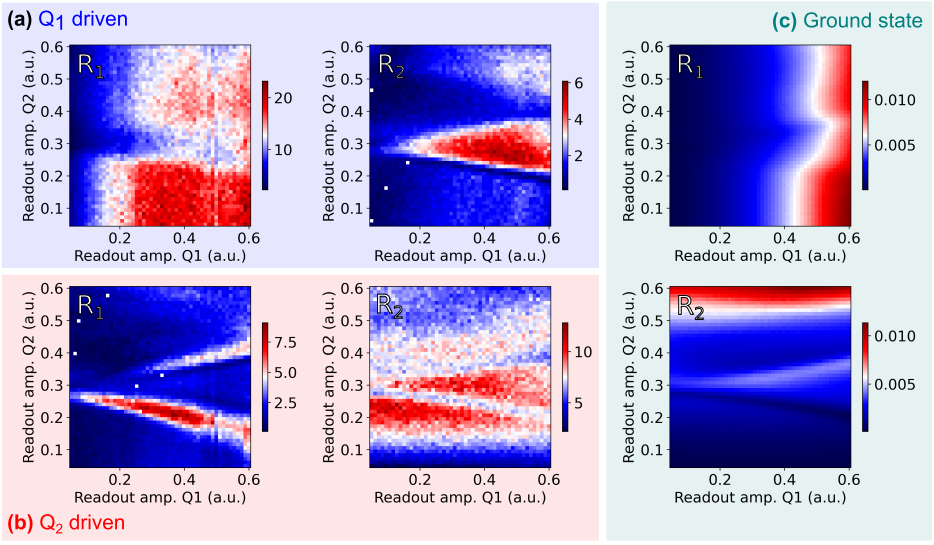

Figure 6.3: Readout crosstalk in two-qubit experiments measured from driving at most one qubit, but reading out both We perform multiplexed readout of two resonators, but only drive Q_1 **((a))** only Q_2 **((b))** or none of them **((c))**. In **(a)** and **(b)**, we plot the signal-to-noise ratio (SNR) of the observed oscillations. Red regions have SNRs and correspond to well visible Rabi oscillations. In these plots, correlations show up as red regions in the resonator which does not have a driven qubit coupeld to it (i.e. **(a)** right and **(b)** left). When not driving any of the qubits, the measured signals show a similar structure **((c))**.

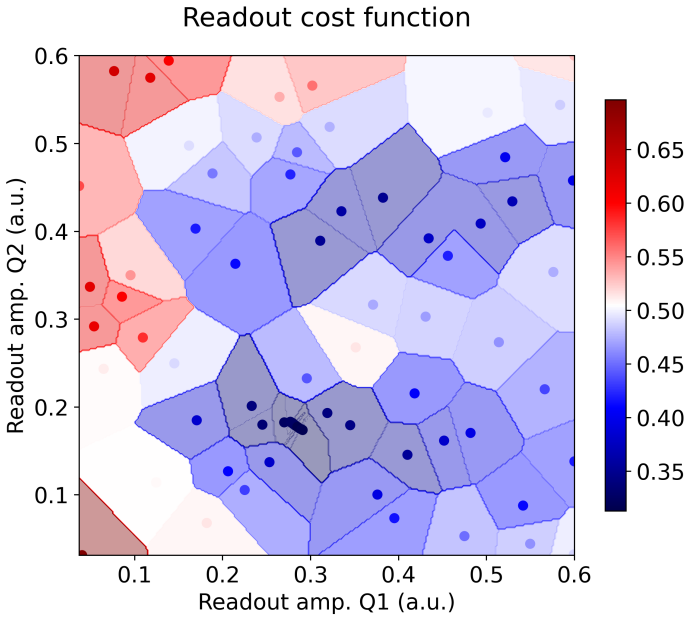

Figure 6.4: Correlation-conscious optimization of two-qubit readout A novel figure of merit consisting of the product of assignment fidelities and the symmetric quantum correlation coefficient of the system is optimized. The parameter space is spanned by the respective reaodut amplitudes of the two resonators. The optimal readout parameters are identified to be $(R_1, R_2) = (0.280, 0.181)$.

6.4 Optimizing readout parameters

The two parameters we change to optimize the readout are chosen to be the two amplitudes of the readout pulses used to measure the two resonators. For a given pair of readout amplitudes (R_1, R_2), detector tomography is employed to extract symmetric quantum correlation coefficients, while assignment fidelity is measured for the computational basis states. To identify optimal readout parameters that balance high assignment fidelity and low correlations, a readout cost function is defined. This function needs to include both assignment fidelities of the two qubits. We choose to use the product of the two assignment fidelities, as this gives a direct physical interpretation of assignment fidelity of the two-qubit computational basis states. Alternatively, the sum may also be used. Next, the symmetric quantum correlation coefficient is used as this contains readout correlation in both directions between the qubits. Finally, we add a scaling parameter, α, which enables us to set

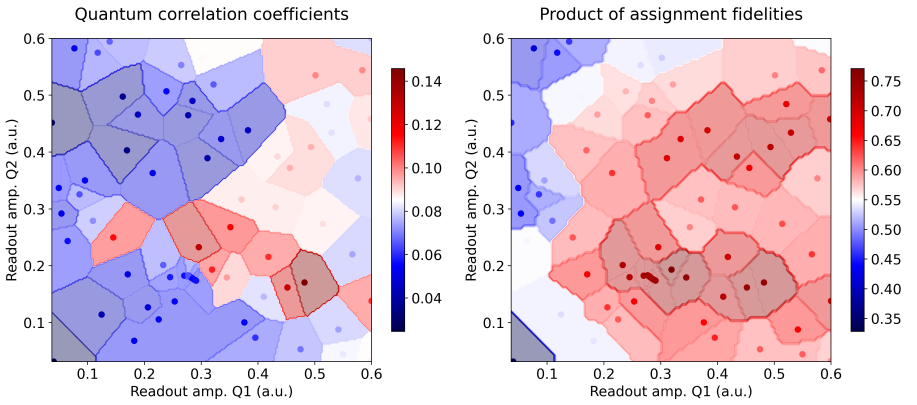

Figure 6.5: Constituents of the correlation-conscious qubit readout metric Left: Symmetric quantum correlation coefficients are low when either of the two readout amplitudes is low and shows a non-trivial behaviour with increasing the readout amplitude for Q1 **Right:** The product of assignment fidelities has a maximum on both spanning axes of the parameters space, therefore the maximum is reached when both R1 and R2 are read out at their respective optimal amplitudes.

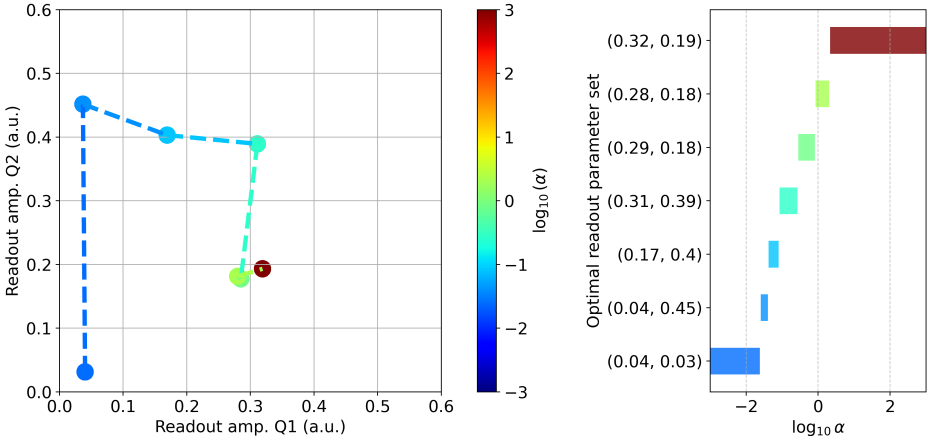

Figure 6.6: Evolution of the optimal operating point based on pre-sampled datapoints as a function of parameter α Very low α values correspond to effectively only minimizing readout correlations, which leads to low readout amplitudes. Values of α much greater than one shift the focus on the optimizer to assignment fidelity, leading it to neglect readout correlations. **Left:** The path of optimal parameters as a function of α for pre-evaluated points. **Right:** The identified optimal readout amplitude pairs are discrete due to the finite number of measured points.

the relative importance of the individual readout variables we want to optimize. Hence, we define the correlation-conscious readout cost function as:

$$G = c_{i\leftrightarrow j} + \alpha\left(1 - \mathcal{F}_1\mathcal{F}_2\right),$$

where $c_{i\leftrightarrow j}$ represents the symmetric quantum correlation coefficient (as defined in Sec. 2.10), $\mathcal{F}_i$ is the assignment fidelity for Q_i, and α is the scaling parameter. The value of α determines the relative importance of achieving high assignment fidelity versus minimizing correlations. For instance:

- If reducing bias is prioritized (e.g., for state reconstruction in quantum simulations with more averages), a small value ($\alpha \ll 1$) is chosen.
- For single-shot readout (e.g., in active reset scenarios), a large value ($\alpha \gg 1$) is preferred.

In this study, $\alpha = 1$ was used for simplicity, with different regimes of α discussed later. A Bayesian optimizer based on Gaussian processes was used to minimize this cost function over 75 iterations, yielding optimal parameters at $(R_1, R_2) = (0.280, 0.181)$. The components of the cost function are shown in Fig. 6.5, where quantum correlation coefficients exhibit similar parameter dependence as computational basis readout crosstalk in Fig. 6.3. This shows that the concepts of readout crosstalk as defined from two-qubit cross-Rabi experiments and readout correlation coefficients are very similar in this case.

Low readout amplitudes reduce correlations but also degrade assignment fidelities due to poor distinguishability of computational basis states. The optimal parameters differ from those obtained by maximizing either assignment fidelity or minimizing correlations alone, highlighting the importance of correlation-aware optimization when crosstalk is present.

6.5 Tracking optimum-readout traces in parameter space

As α is a free parameter in our optimization procedure and was chosen arbitrarily, it is important to disuss the effect it has on optimization. To analyze the influence of α, the cost function was reevaluated for various values of α using previously measured data points. This approach tracked updated minima across parameter space as α was swept over $[10^{-3}, 10^{3}]$. Seven optimal parameter pairs were identified and plotted in Fig. 6.6. Discrete jumps between optima arise from evaluating the

cost function at fixed points; increasing the number of data points would smooth this trajectory. The extrema at $(0.04, 0.03)$ and $(0.32, 0.19)$ correspond to limiting cases where optimization focuses almost exclusively on minimizing correlations or maximizing assignment fidelity, respectively, reflecting the endpoints of the α-dependent trace in parameter space.

7 Conclusion and outlook

This thesis combines three projects focused on mitigating readout errors in quantum state tomography. Our protocol, based on detector tomography, estimates the noisy measurement process using positive operator-valued measures (POVMs). The experiments were conducted on devices with multiple superconducting qubits.

Initially, we tested the readout error mitigation protocol on a single superconducting qubit, benchmarking its ability to mitigate various readout errors. We observed that pure readout noises, such as those from insufficient signal amplification or resonator drive power, can be efficiently mitigated, even in extreme cases, with an infidelity improvement of a factor of 30. This allowed for precise reconstruction of the pre-measurement quantum state. However, mixed readout noises that also affect state preparation can only be mitigated by a constant factor compared to naive state reconstruction. An example of such noise is off-resonant qubit drive. Additionally, errors primarily affecting state preparation, like increased cryostat temperatures, can undermine readout error mitigation in ways not immediately apparent from infidelity saturation in quantum state tomography.

In the second project, we scaled up the experiment to multiple qubits. By efficiently extracting the infidelity convergence of quantum state tomography as a function of shots performed, we introduced a novel readout metric to quantify the information extraction rate from the quantum system. This metric extends beyond assignment fidelity by not being limited to preparing and reading out just the two computational basis states per qubit, and it meaningfully quantifies the rate at which quantum information can be transferred to classical information processable on a conventional computer. We also found that readout correlation coefficients for two-qubit systems do not depend on the strength of readout noise within experimental bounds, allowing them to serve as an independent figure of merit from assignment fidelity. Furthermore, we observed that coherent readout errors in the measurement operator can be induced if laboratory temperature and humidity are not closely controlled.

In the final project, we investigated a weakly detuned system of two qubits, each coupled to a readout resonator sharing a transmission line for microwave measurements. We demonstrated that readout parameter-dependent crosstalk is present and

that crosstalk and correlations are related. To identify ideal operating parameters for two-qubit multiplexed readout that is correlation-conscious, we defined a novel readout metric incorporating both readout correlations and assignment fidelities. We showed that the location of optima in parameter space strongly depends on the relative importance of minimizing correlations and maximizing assignment fidelity. Notably, readout correlations could be reduced by up to a factor of two by choosing appropriate readout parameters without affecting assignment fidelity.

Finally, we highlight four potential future research directions building on this thesis.

Firstly, mapping reconstructed POVMs to real experimental noise sources could provide insights into improving readout hardware or designing superconducting quantum circuits, which is crucial for overcoming the significant hurdle of readout errors in sustained quantum error correction experiments.

Secondly, addressing the challenge of temporal drift in operational parameters could be approached using time-dependent neural networks, such as recurrent neural networks, to track and adjust parameters or post-process data at the single-shot level.

Thirdly, extracting entanglement measures from reconstructed POVMs for two-qubit readout could reveal whether the measurement process can induce entanglement between qubits, which has significant implications for quantum error correction beyond simple readout correlations.

Lastly, in the context of reinforcement learning-based novel entangling gate discovery, readout error-mitigated two- and three-qubit density matrix reconstruction could serve as a valuable tool to understand entanglement mechanisms, particularly when the learning agent operates unsupervised.

Bibliography

[1] F. J. Giessibl: *Advances in atomic force microscopy*. Reviews of Modern Physics **75** (2003), 949–983. DOI: 10.1103/revmodphys.75.949 (cit. on p. 1).

[2] J. Thompson, N. Lawrentschuk, M. Frydenberg, L. Thompson, and P. Stricker: *The role of magnetic resonance imaging in the diagnosis and management of prostate cancer*. BJU International **112** (2013), 6–20. DOI: 10.1111/bju.12381 (cit. on p. 1).

[3] A. Roy and M. Devoret: *Quantum-limited parametric amplification with Josephson circuits in the regime of pump depletion*. Physical Review B **98** (2018). DOI: 10.1103/physrevb.98.045405 (cit. on p. 1).

[4] R. Kleiner, D. Koelle, F. Ludwig, and J. Clarke: *Superconducting quantum interference devices: State of the art and applications*. Proceedings of the IEEE **92** (2004), 1534–1548. DOI: 10.1109/jproc.2004.833655 (cit. on p. 1).

[5] R. P. Feynman: *Simulating physics with computers*. International Journal of Theoretical Physics **21** (1982), 467–488. DOI: 10.1007/bf02650179 (cit. on p. 1).

[6] P. Krantz, M. Kjaergaard, F. Yan, T. P. Orlando, S. Gustavsson, and W. D. Oliver: *A quantum engineer's guide to superconducting qubits*. Applied Physics Reviews **6** (2019). DOI: 10.1063/1.5089550 (cit. on pp. 1, 8, 21).

[7] M. Kjaergaard, M. E. Schwartz, J. Braumüller, P. Krantz, J. I.-J. Wang, S. Gustavsson, and W. D. Oliver: *Superconducting Qubits: Current State of Play*. Annual Review of Condensed Matter Physics **11** (2020), 369–395. DOI: 10.1146/annurev-conmatphys-031119-050605 (cit. on pp. 1, 2, 21, 23).

[8] K. Kubo and H. Goto: *Fast parametric two-qubit gate for highly detuned fixed-frequency superconducting qubits using a double-transmon coupler*. Applied Physics Letters **122** (2023). DOI: 10.1063/5.0138699 (cit. on p. 1).

[9] Y. Ye, J. B. Kline, S. Chen, A. Yen, and K. P. O'Brien: *Ultrafast superconducting qubit readout with the quarton coupler*. Science Advances **10** (2024). DOI: 10.1126/sciadv.ado9094 (cit. on p. 1).

[10] A. Wallraff, D. I. Schuster, A. Blais, L. Frunzio, J. Majer, M. H. Devoret, S. M. Girvin, and R. J. Schoelkopf: *Approaching Unit Visibility for Control of a Superconducting Qubit with Dispersive Readout*. Physical Review Letters **95** (2005). DOI: 10.1103/physrevlett.95.060501 (cit. on p. 2).

[11] M. Jerger, S. Poletto, P. Macha, U. Hübner, E. Il'ichev, and A. V. Ustinov: *Frequency division multiplexing readout and simultaneous manipulation of an array of flux qubits*. Applied Physics Letters **101** (2012), 042604. DOI: 10.1063/1.4739454 (cit. on pp. 2, 25, 61).

[12] A. W. R. Smith, K. E. Khosla, C. N. Self, and M. S. Kim: *Qubit readout error mitigation with bit-flip averaging*. Science Advances **7** (2021). DOI: 10.1126/sciadv.abi8009 (cit. on p. 2).

[13] Y. Chen, M. Farahzad, S. Yoo, and T.-C. Wei: *Detector tomography on IBM quantum computers and mitigation of an imperfect measurement*. Physical Review A **100** (2019). DOI: 10.1103/physreva.100.052315 (cit. on p. 2).

[14] F. B. Maciejewski, Z. Zimborás, and M. Oszmaniec: *Mitigation of readout noise in near-term quantum devices by classical post-processing based on detector tomography*. Quantum **4** (2020), 257. DOI: 10.22331/q-2020-04-24-257 (cit. on pp. 2, 10, 35).

[15] F. B. Maciejewski, F. Baccari, Z. Zimborás, and M. Oszmaniec: *Modeling and mitigation of cross-talk effects in readout noise with applications to the Quantum Approximate Optimization Algorithm*. Quantum **5** (2021), 464. DOI: 10.22331/q-2021-06-01-464 (cit. on pp. 2, 10, 18, 47, 61).

[16] J. S. Lundeen, A. Feito, H. Coldenstrodt-Ronge, K. L. Pregnell, C. Silberhorn, T. C. Ralph, J. Eisert, M. B. Plenio, and I. A. Walmsley: *Tomography of quantum detectors*. Nature Physics **5** (2008), 27–30. DOI: 10.1038/nphys1133 (cit. on pp. 2, 13, 35).

[17] B. Lienhard et al.: *Deep-Neural-Network Discrimination of Multiplexed Superconducting-Qubit States*. Physical Review Applied **17** (2022). DOI: 10.1103/physrevapplied.17.014024 (cit. on pp. 2, 25, 26).

[18] A. S. Aasen, A. Di Giovanni, H. Rotzinger, A. V. Ustinov, and M. Gärttner: *Readout error mitigated quantum state tomography tested on superconducting qubits*. Communications Physics **7** (2024). DOI: 10.1038/s42005-024-01790-8 (cit. on pp. 5, 10, 13, 15–18, 35, 38, 50).

[19] A. Di Giovanni, A. S. Aasen, J. Lisenfeld, M. Gärttner, H. Rotzinger, and A. V. Ustinov: *Multiplexed qubit readout quality metric beyond assignment fidelity* (2025). DOI: 10.48550/ARXIV.2502.08589 (cit. on pp. 5, 47, 61).

[20] M. A. Nielsen and I. L. Chuang: *Quantum Computation and Quantum Information*. Cambridge University Press, 2012. DOI: 10.1017/cbo9780511976667 (cit. on pp. 5, 15, 16).

[21] F. Bloch: *Nuclear Induction*. Physical Review **70** (1946), 460–474. DOI: 10.1103/physrev.70.460 (cit. on p. 8).

[22] R. P. Feynman, F. L. Vernon, and R. W. Hellwarth: *Geometrical Representation of the Schrödinger Equation for Solving Maser Problems*. Journal of Applied Physics **28** (1957), 49–52. DOI: 10.1063/1.1722572 (cit. on p. 8).

[23] J. Johansson, P. Nation, and F. Nori: *QuTiP: An open-source Python framework for the dynamics of open quantum systems*. Computer Physics Communications **183** (2012), 1760–1772. DOI: 10.1016/j.cpc.2012.02.021 (cit. on p. 8).

[24] J. Johansson, P. Nation, and F. Nori: *QuTiP 2: A Python framework for the dynamics of open quantum systems*. Computer Physics Communications **184** (2013), 1234–1240. DOI: 10.1016/j.cpc.2012.11.019 (cit. on p. 8).

[25] L. Chirolli and G. Burkard: *Decoherence in solid-state qubits*. Advances in Physics **57** (2008), 225–285. DOI: 10.1080/00018730802218067 (cit. on p. 8).

[26] J. Lisenfeld, A. Bilmes, S. Matityahu, S. Zanker, M. Marthaler, M. Schechter, G. Schön, A. Shnirman, G. Weiss, and A. V. Ustinov: *Decoherence spectroscopy with individual two-level tunneling defects*. Scientific Reports **6** (2016). DOI: 10.1038/srep23786 (cit. on p. 8).

[27] S. J. Devitt, W. J. Munro, and K. Nemoto: *Quantum error correction for beginners*. Reports on Progress in Physics **76** (2013), 076001. DOI: 10.1088/0034-4885/76/7/076001 (cit. on p. 9).

[28] *Quantum Error Correction*. Cambridge University Press, 2013. DOI: 10.1017/cbo9781139034807 (cit. on p. 9).

[29] J. Roffe: *Quantum error correction: an introductory guide*. Contemporary Physics **60** (2019), 226–245. DOI: 10.1080/00107514.2019.1667078 (cit. on p. 9).

[30] J. Chiaverini, D. Leibfried, T. Schaetz, M. D. Barrett, R. B. Blakestad, J. Britton, W. M. Itano, J. D. Jost, E. Knill, C. Langer, R. Ozeri, and D. J. Wineland: *Realization of quantum error correction*. Nature **432** (2004), 602–605. DOI: 10.1038/nature03074 (cit. on p. 9).

[31] E. Knill and R. Laflamme: *Theory of quantum error-correcting codes*. Physical Review A **55** (1997), 900–911. DOI: 10.1103/physreva.55.900 (cit. on p. 9).

[32] Y. Zhao et al.: *Realization of an Error-Correcting Surface Code with Superconducting Qubits*. Physical Review Letters **129** (2022). DOI: 10.1103/physrevlett.129.030501 (cit. on p. 9).

[33] R. Acharya et al.: *Suppressing quantum errors by scaling a surface code logical qubit*. Nature **614** (2023), 676–681. DOI: 10.1038/s41586-022-05434-1 (cit. on p. 9).

[34] R. Acharya et al.: *Quantum error correction below the surface code threshold*. Nature **638** (2024), 920–926. DOI: 10.1038/s41586-024-08449-y (cit. on p. 9).

[35] M. R. Geller and Z. Zhou: *Efficient error models for fault-tolerant architectures and the Pauli twirling approximation*. Physical Review A **88** (2013). DOI: 10.1103/physreva.88.012314 (cit. on p. 9).

[36] Z. Cai and S. C. Benjamin: *Constructing Smaller Pauli Twirling Sets for Arbitrary Error Channels*. Scientific Reports **9** (2019). DOI: 10.1038/s41598-019-46722-7 (cit. on p. 9).

[37] A. Katabarwa and M. R. Geller: *Logical error rate in the Pauli twirling approximation*. Scientific Reports **5** (2015). DOI: 10.1038/srep14670 (cit. on p. 9).

[38] G. Liu, Z. Xie, Z. Xu, and X. Ma: *Group twirling and noise tailoring for multiqubit controlled phase gates*. Physical Review Research **6** (2024). DOI: 10.1103/physrevresearch.6.043221 (cit. on p. 9).

[39] K. Temme, S. Bravyi, and J. M. Gambetta: *Error Mitigation for Short-Depth Quantum Circuits*. Physical Review Letters **119** (2017). DOI: 10.1103/physrevlett.119.180509 (cit. on p. 10).

[40] M. A. Wahl, A. Mari, N. Shammah, W. J. Zeng, and G. S. Ravi: *Zero Noise Extrapolation on Logical Qubits by Scaling the Error Correction Code Distance*. *2023 IEEE International Conference on Quantum Computing and Engineering (QCE)*. IEEE, 2023, pp. 888–897. DOI: 10.1109/qce57702.2023.00103 (cit. on p. 10).

[41] V. R. Pascuzzi, A. He, C. W. Bauer, W. A. de Jong, and B. Nachman: *Computationally efficient zero-noise extrapolation for quantum-gate-error mitigation*. Physical Review A **105** (2022). DOI: 10.1103/physreva.105.042406 (cit. on p. 10).

[42] K. Schultz, R. LaRose, A. Mari, G. Quiroz, N. Shammah, B. D. Clader, and W. J. Zeng: *Impact of time-correlated noise on zero-noise extrapolation*. Physical Review A **106** (2022). DOI: 10.1103/physreva.106.052406 (cit. on p. 10).

[43] A. He, B. Nachman, W. A. de Jong, and C. W. Bauer: *Zero-noise extrapolation for quantum-gate error mitigation with identity insertions*. Physical Review A **102** (2020). DOI: 10.1103/physreva.102.012426 (cit. on p. 10).

[44] T. Giurgica-Tiron, Y. Hindy, R. LaRose, A. Mari, and W. J. Zeng: *Digital zero noise extrapolation for quantum error mitigation*. *2020 IEEE International Conference on Quantum Computing and Engineering (QCE)*. IEEE, 2020, pp. 306–316. DOI: 10.1109/qce49297.2020.00045 (cit. on p. 10).

[45] K. Vogel and H. Risken: *Determination of quasiprobability distributions in terms of probability distributions for the rotated quadrature phase*. Physical Review A **40** (1989), 2847–2849. DOI: 10.1103/physreva.40.2847 (cit. on p. 12).

[46] R. Blume-Kohout: *Optimal, reliable estimation of quantum states*. New Journal of Physics **12** (2010), 043034. DOI: 10.1088/1367-2630/12/4/043034 (cit. on pp. 13, 45).

[47] V. Gebhart, R. Santagati, A. A. Gentile, E. M. Gauger, D. Craig, N. Ares, L. Banchi, F. Marquardt, L. Pezzè, and C. Bonato: *Learning quantum systems*. Nature Reviews Physics **5** (2023), 141–156. DOI: 10.1038/s42254-022-00552-1 (cit. on p. 13).

[48] A. I. Lvovsky: *Iterative maximum-likelihood reconstruction in quantum homodyne tomography*. Journal of Optics B: Quantum and Semiclassical Optics **6** (2004), S556–S559. DOI: 10.1088/1464-4266/6/6/014 (cit. on pp. 13, 45).

[49] J. Fiurášek: *Maximum-likelihood estimation of quantum measurement*. Physical Review A **64** (2001). DOI: 10.1103/physreva.64.024102 (cit. on p. 14).

[50] A. Di Giovanni, A. S. Aasen, M. Gärttner, H. Rotzinger, and A. V. Ustinov: *Correlation-conscious optimization of multiplexed qubit readout*. In preparation (2025) (cit. on pp. 15, 48, 50).

[51] J. Tuziemski, F. B. Maciejewski, J. Majsak, O. Słowik, M. Kotowski, K. Kowalczyk-Murynka, P. Podziemski, and M. Oszmaniec: *Efficient reconstruction, benchmarking and validation of cross-talk models in readout noise in near-term quantum devices*. 2023. DOI: 10.48550/ARXIV.2311.10661 (cit. on pp. 18, 45, 47, 61).

[52] L. Chen et al.: *Transmon qubit readout fidelity at the threshold for quantum error correction without a quantum-limited amplifier*. npj Quantum Information **9** (2023). DOI: 10.1038/s41534-023-00689-6 (cit. on pp. 19, 47, 61).

[53] S. S. Elder, C. S. Wang, P. Reinhold, C. T. Hann, K. S. Chou, B. J. Lester, S. Rosenblum, L. Frunzio, L. Jiang, and R. J. Schoelkopf: *High-Fidelity Measurement of Qubits Encoded in Multilevel Superconducting Circuits*. Physical Review X **10** (2020). DOI: 10.1103/physrevx.10.011001 (cit. on pp. 19, 47, 61).

[54] J. Heinsoo, C. K. Andersen, A. Remm, S. Krinner, T. Walter, Y. Salathé, S. Gasparinetti, J.-C. Besse, A. Potočnik, A. Wallraff, and C. Eichler: *Rapid High-fidelity Multiplexed Readout of Superconducting Qubits*. Physical Review Applied **10** (2018). DOI: 10.1103/physrevapplied.10.034040 (cit. on pp. 19, 25, 47, 61).

[55] B. R. Johnson, M. D. Reed, A. A. Houck, D. I. Schuster, L. S. Bishop, E. Ginossar, J. M. Gambetta, L. DiCarlo, L. Frunzio, S. M. Girvin, and R. J. Schoelkopf: *Quantum non-demolition detection of single microwave photons in a circuit*. Nature Physics **6** (2010), 663–667. DOI: 10.1038/nphys1710 (cit. on p. 19).

[56] J. Yoneda, K. Takeda, A. Noiri, T. Nakajima, S. Li, J. Kamioka, T. Kodera, and S. Tarucha: *Quantum non-demolition readout of an electron spin in silicon*. Nature Communications **11** (2020). DOI: 10.1038/s41467-020-14818-8 (cit. on p. 19).

[57] J. Gambetta, W. A. Braff, A. Wallraff, S. M. Girvin, and R. J. Schoelkopf: *Protocols for optimal readout of qubits using a continuous quantum nondemolition measurement*. Physical Review A **76** (2007). DOI: 10.1103/physreva.76.012325 (cit. on p. 19).

[58] N. Didier, J. Bourassa, and A. Blais: *Fast Quantum Nondemolition Readout by Parametric Modulation of Longitudinal Qubit-Oscillator Interaction*. Physical Review Letters **115** (2015). DOI: 10.1103/physrevlett.115.203601 (cit. on p. 19).

[59] H. Zhang, S. Chakram, T. Roy, N. Earnest, Y. Lu, Z. Huang, D. K. Weiss, J. Koch, and D. I. Schuster: *Universal Fast-Flux Control of a Coherent, Low-Frequency Qubit*. Physical Review X **11** (2021). DOI: 10.1103/physrevx.11.011010 (cit. on p. 21).

[60] A. Anferov, F. Wan, S. P. Harvey, J. Simon, and D. I. Schuster: *A Millimeter-Wave Superconducting Qubit*. 2024. DOI: 10.48550/ARXIV.2411.11170 (cit. on p. 21).

[61] R. Radebaugh and J. Siegwarth: *Dilution refrigerator technology*. Cryogenics **11** (1971), 368–384. DOI: 10.1016/0011-2275(71)90037-3 (cit. on p. 21).

[62] H. Zu, W. Dai, and A. de Waele: *Development of dilution refrigerators—A review*. Cryogenics **121** (2022), 103390. DOI: 10.1016/j.cryogenics.2021.103390 (cit. on p. 21).

[63] J. C. Wheatley, O. E. Vilches, and W. R. Abel: *Principles and methods of dilution refrigeration*. Physics Physique Fizika **4** (1968), 1–64. DOI: 10.1103/physicsphysiquefizika.4.1 (cit. on p. 21).

[64] M. H. Devoret and J. M. Martinis: *Course 12 Superconducting qubits. Quantum Entanglement and Information Processing, École d' été de Physique des Houches Session LXXIX*. Elsevier, 2004, pp. 443–485. DOI: 10.1016/s0924-8099(03)80036-7 (cit. on p. 23).

[65] I. Siddiqi: *Engineering high-coherence superconducting qubits*. Nature Reviews Materials **6** (2021), 875–891. DOI: 10.1038/s41578-021-00370-4 (cit. on p. 23).

[66] E. Jeffrey et al.: *Fast Accurate State Measurement with Superconducting Qubits*. Physical Review Letters **112** (2014). DOI: 10.1103/physrevlett.112.190504 (cit. on p. 23).

[67] A. M. Gunyhó, S. Kundu, J. Ma, W. Liu, S. Niemelä, G. Catto, V. Vadimov, V. Vesterinen, P. Singh, Q. Chen, and M. Möttönen: *Single-shot readout of a superconducting qubit using a thermal detector*. Nature Electronics **7** (2024), 288–298. DOI: 10.1038/s41928-024-01147-7 (cit. on p. 23).

[68] G. Arnold, T. Werner, R. Sahu, L. N. Kapoor, L. Qiu, and J. M. Fink: *All-optical superconducting qubit readout*. Nature Physics (2025). DOI: 10.1038/s41567-024-02741-4 (cit. on p. 23).

[69] C. Macklin, K. O'Brien, D. Hover, M. E. Schwartz, V. Bolkhovsky, X. Zhang, W. D. Oliver, and I. Siddiqi: *A near–quantum-limited Josephson traveling-wave parametric amplifier*. Science **350** (2015), 307–310. DOI: 10.1126/science.aaa8525 (cit. on pp. 23, 27, 55).

[70] J. Majer, J. M. Chow, J. M. Gambetta, J. Koch, B. R. Johnson, J. A. Schreier, L. Frunzio, D. I. Schuster, A. A. Houck, A. Wallraff, A. Blais, M. H. Devoret, S. M. Girvin, and R. J. Schoelkopf: *Coupling superconducting qubits via a cavity bus*. Nature **449** (2007), 443–447. DOI: 10.1038/nature06184 (cit. on p. 25).

[71] Y. Chen et al.: *Multiplexed dispersive readout of superconducting phase qubits*. Applied Physics Letters **101** (2012). DOI: 10.1063/1.4764940 (cit. on p. 25).

[72] J. M. Hornibrook, J. I. Colless, A. C. Mahoney, X. G. Croot, S. Blanvillain, H. Lu, A. C. Gossard, and D. J. Reilly: *Frequency multiplexing for readout of spin qubits*. Applied Physics Letters **104** (2014). DOI: 10.1063/1.4868107 (cit. on p. 25).

[73] V. Schmitt, X. Zhou, K. Juliusson, B. Royer, A. Blais, P. Bertet, D. Vion, and D. Esteve: *Multiplexed readout of transmon qubits with Josephson bifurcation amplifiers*. Physical Review A **90** (2014). DOI: 10.1103/physreva.90.062333 (cit. on p. 25).

[74] D. Pitsun, A. Sultanov, I. Novikov, E. Mutsenik, B. Ivanov, A. Matanin, V. Polozov, E. Malevannaya, A. Ivanov, G. Fedorov, K. Delfanazari, I. Rodionov, and E. Il'ichev: *Cross Coupling of a Solid-State Qubit to an Input Signal due to Multiplexed Dispersive Readout*. Physical Review Applied **14** (2020). DOI: 10.1103/physrevapplied.14.054059 (cit. on p. 25).

[75] H.-S. Yeo, S. Woo, J. Kim, Y. Kim, B. Choi, G. Choi, J. Choi, S. K. Lee, W. Song, and Y. Chong: *High-Fidelity Multiplexed Single-Shot Readout for Transmon Qubits With High-Power Measurement*. IEEE Transactions on Applied Superconductivity **33** (2023), 1–5. DOI: 10.1109/tasc.2023.3254485 (cit. on p. 25).

[76] B. Nachman, M. Urbanek, W. A. de Jong, and C. W. Bauer: *Unfolding quantum computer readout noise*. npj Quantum Information **6** (2020). DOI: 10.1038/s41534-020-00309-7 (cit. on p. 35).

[77] S. Bravyi, S. Sheldon, A. Kandala, D. C. Mckay, and J. M. Gambetta: *Mitigating measurement errors in multiqubit experiments*. Physical Review A **103** (2021). DOI: 10.1103/physreva.103.042605 (cit. on p. 35).

[78] H. Kwon and J. Bae: *A Hybrid Quantum-Classical Approach to Mitigating Measurement Errors in Quantum Algorithms*. IEEE Transactions on Computers **70** (2021), 1401–1411. DOI: 10.1109/tc.2020.3009664 (cit. on p. 35).

[79] F. Mezzadri: *How to generate random matrices from the classical compact groups* (2006). DOI: 10.48550/ARXIV.MATH-PH/0609050 (cit. on pp. 35, 37, 50).

[80] A. Schneider: *Quantum Sensing Experiments with Superconducting Qubits* (2020). DOI: 10.5445/IR/1000117442 (cit. on p. 36).

[81] D. C. McKay, C. J. Wood, S. Sheldon, J. M. Chow, and J. M. Gambetta: *Efficient Z gates for quantum computing*. Physical Review A **96** (2017). DOI: 10.1103/physreva.96.022330 (cit. on p. 37).

[82] M. R. Geller and M. Sun: *Toward efficient correction of multiqubit measurement errors: pair correlation method*. Quantum Science and Technology **6** (2021), 025009. DOI: 10.1088/2058-9565/abd5c9 (cit. on p. 38).

[83] D. Greenbaum: *Introduction to Quantum Gate Set Tomography*. 2015. DOI: 10.48550/ARXIV.1509.02921 (cit. on p. 38).

[84] J. Y. Qiu et al.: *Broadband squeezed microwaves and amplification with a Josephson travelling-wave parametric amplifier*. Nature Physics (2023). DOI: 10.1038/s41567-022-01929-w (cit. on p. 40).

[85] J. J. Burnett, A. Bengtsson, M. Scigliuzzo, D. Niepce, M. Kudra, P. Delsing, and J. Bylander: *Decoherence benchmarking of superconducting qubits*. npj Quantum Information **5** (2019). DOI: 10.1038/s41534-019-0168-5 (cit. on p. 42).

[86] G. Catelani, S. E. Nigg, S. M. Girvin, R. J. Schoelkopf, and L. I. Glazman: *Decoherence of superconducting qubits caused by quasiparticle tunneling*. Physical Review B **86** (2012). DOI: 10.1103/physrevb.86.184514 (cit. on p. 42).

[87] S. M. Meißner, A. Seiler, J. Lisenfeld, A. V. Ustinov, and G. Weiss: *Probing individual tunneling fluctuators with coherently controlled tunneling systems*. Physical Review B **97** (2018). DOI: 10.1103/physrevb.97.180505 (cit. on p. 44).

[88] J. Cotler and F. Wilczek: *Quantum Overlapping Tomography*. Physical Review Letters **124** (2020). DOI: 10.1103/physrevlett.124.100401 (cit. on p. 45).

[89] A. S. Aasen, A. Di Giovanni, H. Rotzinger, A. V. Ustinov, and M. Gärttner: *Scalable readout error mitigation*. In preparation (2025) (cit. on pp. 45, 47).

[90] T. Walter, P. Kurpiers, S. Gasparinetti, P. Magnard, A. Potočnik, Y. Salathé, M. Pechal, M. Mondal, M. Oppliger, C. Eichler, and A. Wallraff: *Rapid High-Fidelity Single-Shot Dispersive Readout of Superconducting Qubits*. Physical Review Applied **7** (2017). DOI: 10.1103/physrevapplied.7.054020 (cit. on pp. 47, 55).

[91] D. Gusenkova et al.: *Quantum Nondemolition Dispersive Readout of a Superconducting Artificial Atom Using Large Photon Numbers*. Physical Review Applied **15** (2021). DOI: 10.1103/physrevapplied.15.064030 (cit. on p. 47).

[92] T. Picot, R. Schouten, C. J. P. M. Harmans, and J. E. Mooij: *Quantum Nondemolition Measurement of a Superconducting Qubit in the Weakly Projective Regime*. Physical Review Letters **105** (2010). DOI: 10.1103/physrevlett.105.040506 (cit. on p. 47).

[93] R. Dassonneville, T. Ramos, V. Milchakov, L. Planat, É. Dumur, F. Foroughi, J. Puertas, S. Leger, K. Bharadwaj, J. Delaforce, C. Naud, W. Hasch-Guichard, J. J. García-Ripoll, N. Roch, and O. Buisson: *Fast High-Fidelity Quantum Nondemolition Qubit Readout via a Nonperturbative Cross-Kerr Coupling*. Physical Review X **10** (2020). DOI: 10.1103/physrevx.10.011045 (cit. on p. 47).

[94] P. C. de Groot, A. F. van Loo, J. Lisenfeld, R. N. Schouten, A. Lupaşcu, C. J. P. M. Harmans, and J. E. Mooij: *Low-crosstalk bifurcation detectors for coupled flux qubits*. Applied Physics Letters **96** (2010). DOI: 10.1063/1.3367875 (cit. on p. 48).

[95] T. Thorbeck, A. Eddins, I. Lauer, D. T. McClure, and M. Carroll: *Two-Level-System Dynamics in a Superconducting Qubit Due to Background Ionizing Radiation*. PRX Quantum **4** (2023). DOI: 10.1103/prxquantum.4.020356 (cit. on p. 48).

[96] S. Kono, J. Pan, M. Chegnizadeh, X. Wang, A. Youssefi, M. Scigliuzzo, and T. J. Kippenberg: *Mechanically induced correlated errors on superconducting qubits with relaxation times exceeding 0.4 ms*. Nature Communications **15** (2024). DOI: 10.1038/s41467-024-48230-3 (cit. on p. 48).

[97] Y. Kim, A. Morvan, L. B. Nguyen, R. K. Naik, C. Jünger, L. Chen, J. M. Kreikebaum, D. I. Santiago, and I. Siddiqi: *High-fidelity three-qubit iToffoli gate for fixed-frequency superconducting qubits*. Nature Physics **18** (2022), 783–788. DOI: 10.1038/s41567-022-01590-3 (cit. on p. 50).

[98] C. W. Warren et al.: *Extensive characterization and implementation of a family of three-qubit gates at the coherence limit*. npj Quantum Information **9** (2023). DOI: 10.1038/s41534-023-00711-x (cit. on p. 50).

[99] T. Itoko, M. Malekakhlagh, N. Kanazawa, and M. Takita: *Three-qubit parity gate via simultaneous cross-resonance drives*. Physical Review Applied **21** (2024). DOI: 10.1103/physrevapplied.21.034018 (cit. on p. 50).

[100] P. Duan, Z.-F. Chen, Q. Zhou, W.-C. Kong, H.-F. Zhang, and G.-P. Guo: *Mitigating Crosstalk-Induced Qubit Readout Error with Shallow-Neural-Network Discrimination*. Physical Review Applied **16** (2021). DOI: 10.1103/physrevapplied.16.024063 (cit. on p. 61).

[101] L. A. Martinez, Y. J. Rosen, and J. L. DuBois: *Improving qubit readout with hidden Markov models*. Physical Review A **102** (2020). DOI: 10.1103/physreva.102.062426 (cit. on p. 61).

[102] P. A. Spring, L. Milanovic, Y. Sunada, S. Wang, A. F. van Loo, S. Tamate, and Y. Nakamura: *Fast multiplexed superconducting qubit readout with intrinsic Purcell filtering*. 2024. DOI: 10.48550/ARXIV.2409.04967 (cit. on p. 61).

[103] P. I. Frazier: *A Tutorial on Bayesian Optimization*. 2018. DOI: 10.48550/ARXIV.1807.02811 (cit. on p. 61).

List of Publications

[1] A. S. Aasen, A. Di Giovanni, H. Rotzinger, A. V. Ustinov, and M. Gärttner: *Readout error mitigated quantum state tomography tested on superconducting qubits*. Communications Physics **7** (2024). DOI: 10.1038/s42005-024-01790-8.

[2] A. Di Giovanni, A. S. Aasen, J. Lisenfeld, M. Gärttner, H. Rotzinger, and A. V. Ustinov: *Multiplexed qubit readout quality metric beyond assignment fidelity* (2025). DOI: 10.48550/ARXIV.2502.08589.

[3] A. Di Giovanni, A. S. Aasen, M. Gärttner, H. Rotzinger, and A. V. Ustinov: *Correlation-conscious optimization of multiplexed qubit readout*. In preparation (2025).

[4] A. S. Aasen, A. Di Giovanni, H. Rotzinger, A. V. Ustinov, and M. Gärttner: *Scalable readout error mitigation*. In preparation (2025).

Appendix

A Data and code repositories

The processed data used in this thesis is partially available at:

https://publikationen.bibliothek.kit.edu/1000173044 The code developed by Adrian Aasen for this project can be found at

https://github.com/AdrianAasen/EMQST.

For further data or information, please contact the author directly.

Acknowledgements

First, I would like to express gratefulness not for anyone in particular, but generally for Life, that made it possible for me to experience and learn a lot during my time at KIT. Sometimes this meant laughing, sometimes it meant crying, but mostly it meant doing Science.

When it comes to people, I would like to thank my advisor Alexey, who gave me this opportunity at KIT and allowed - nay, motivated me to pursue any ideas whatsoever in the Lab. I hope that I will be able to convince you during the defence, that I am not just doing statistics :) I would also like to thank my day-to-day advisor, Hannes, who not only gave me valuable academic guidance week after week, but was also very present in the social aspects of the group - I will miss the good discussions in mensa and your office.

Thank you, Jürgen, for taking the time to explain to me in the very beginning how a qubit worked, what microwaves were and what a mathematical Physicist should do when he finds himself in a lab with cryostats and electronics. And, of course, thank you for all the remaining discussions!

Nico, chief financial advisor - thanks for the heads up on $SMCI. Please consider getting yourself a *real* iPhone, one that is *special edition*. Drop me a message when someone builds a phase slip nanowire transistor based amplifier, I will invite you for a beer.

Benedikt, Markus, Jakob, Urs, Thilo, and the recent newcomers to PhD life in our group - keep up the good work (and Make PHI Great Again). Dream big, fabricate bigger, and enjoy your time here.

Alex and Hossam - Thanks a lot for your continous *censored*, without which I surely would not have made it through. I wish you good luck and sufficient energy for the last push to join me on the other side. As usual, we meet in the gym tomorrow at 8:00 a.m. :)

Lukas - I thank you for your invested time that allowed us to explore the region around us, as well as your continuous upbeatness. Your worldview has strongly affected mine and for that I am grateful.

Karo - your worldview has not strongly affected mine, and for that I am also grateful ;) But far more than that, I thank you for teaching me to put things into perspective. The train always stops somewhere, and it is our job to make the most out of it and not be scared. Among many smart guys, you were also wise.

Tek and Jacob - your support and friendship is invaluable. Looking forward to joining you in Oxford soon!

Thank you to my parents and brother who were there to support me all the way. Family goes a long way. I love you all.

Finally, thank you to all my wonderful friends, colleagues and co-workers who really made these years worth it.

Thank you Claudia and Steffi for sorting out all matters that are too complicated for a Physicist to deal with.

Thank you Adrian and Martin for teaching me a lot about theoretical Physics. Although I think that in the end, we can all agree that sometimes <100 qubit systems can also be interesting enough to write a few PhDs about ;)

Finally, I would like to thank the person who unlocked the interest and love for quantum information processing and quantum computing in me - without whom I most probably would not have started this PhD: Prof. Crispin Barnes. It was a privilege to have had the opportunity to listen to your lectures.

> "Remember to look up at the stars and not down at your feet. Try to make sense of what you see and wonder about what makes the universe exist."
>
> – Stephen Hawking

Karlsruhe, 9 May 2025 Andras Di Giovanni